Article:
Doherty, TAS, Nagane, S, Kubicki, DJ et al. (18 more authors) (2021) Stabilized tilted-octahedra halide perovskites inhibit local formation of performance-limiting phases. Science, 374 (6575). pp. 1598-1605. ISSN 0036-8075

https://doi.org/10.1126/science.abl4890

Title: Stabilized tilted-octahedra halide perovskites inhibit local formation of performance-limiting phases

Authors:

Tiarnan A.S. Doherty[1†], Satyawan Nagane[1†], Dominik J. Kubicki[1,2], Young-Kwang Jung[3], Duncan N. Johnstone[4], Affan N. Iqbal[1,5], Dengyang Guo[1,5], Kyle Frohna[1], Mohsen Danaie[6,7], Elizabeth M. Tennyson[1], Stuart Macpherson[1], Anna Abfalterer[1], Miguel Anaya[1,5], Yu-Hsien Chiang[1], Phillip Crout[4], Francesco Simone Ruggeri[8], Sean Collins[9], Clare P. Grey[2], Aron Walsh[3,10], Paul A. Midgley[4], Samuel D. Stranks[1,5*]

Affiliations:

[1]Department of Physics, Cavendish Laboratory, University of Cambridge; Cambridge, UK

[2]Yusuf Hamied Department of Chemistry, University of Cambridge; Lensfield Road, Cambridge, UK

[3]Department of Materials Science and Engineering, Yonsei University; Seoul, Korea

[4]Department of Materials Science and Metallurgy, University of Cambridge; Cambridge, UK

[5]Department of Chemical Engineering and Biotechnology, University of Cambridge; Cambridge, UK

[6]Electron Physical Science Imaging Centre, Diamond Light Source Ltd; Didcot, UK

[7]Department of Materials, University of Oxford; Oxford, UK

[8]Laboratory of Organic and Physical Chemistry, Wageningen University and Research, the Netherlands

[9]School of Chemical and Process Engineering & School of Chemistry, University of Leeds; Leeds, UK

[10]Department of Materials, Imperial College London; London, UK

† These authors contributed equally.

*sds65@cam.ac.uk

Abstract: Stabilization of photoactive formamidinium (FA)-based halide perovskites for perovskite photovoltaics has focused on growth of cubic α-$FAPbI_3$ phases by empirically alloying with Cs, methylammonium (MA) cations, or both. We show that such stabilized FA-rich perovskites are non-cubic and exhibit octahedral tilting at room temperature of magnitude ~2°. This tilting, only resolvable with local nanostructure characterization techniques, imparts

phase stability by frustrating transitions from photoactive to hexagonal phases. Although the bulk phase appears stable when examined macroscopically, heterogeneous cation distributions allow microscopically unstable regions to form which transition to hexagonal polytypes, leading to local trap-assisted performance losses and photo-instabilities. We engineered an octahedral tilt into pure α-$FAPbI_3$ thin films without any cation alloying with surface-bound ethylenediaminetetraacetic acid. The templated photoactive $FAPbI_3$ film was extremely stable against thermal, environmental, and light stressors.

One Sentence Summary: Octahedral tilting stabilizes formamidinium-based photoactive perovskites, preventing formation of local sites that trap charge carriers and realizes stable formamidinium lead iodide perovskites thin films entirely free of cation additives and robust to external light, environmental and thermal stressors.

Main Text: Although early perovskite solar cells primarily used methylammonium (MA)-based absorber layers, formamidinium (FA)-based perovskites have much greater thermal stability. However, $FAPbI_3$ is challenging both to fabricate and stabilize as the photoactive cubic phase (α-$FAPbI_3$) comprising corner-sharing PbI_6 octahedra is only stable at temperatures > 150°C, where it is entropically stabilized by the reorientating FA cations (*1*). At room temperature the energy barrier is readily overcome and the material rapidly transitions to wide bandgap, face-sharing hexagonal polytypes, such as the 2H δ-phase, 4H or 6H phases (*2*, *3*). Alloying FA with Cs^+, MA, or both on the A site cation of the ABX_3 perovskite structure can stabilize photoactive $FAPbI_3$-like cubic structures at room temperature. For example, perovskite solar cells fabricated with $Cs_{0.05}FA_{0.78}MA_{0.17}Pb(I_{0.83}Br_{0.17})_3$ (triple-cation) or those comprised of $FAPbI_3$ alloyed with $MAPbBr_3$ perovskites have achieved high power conversion efficiencies (PCEs) with greatly enhanced reproducibility and ambient stability relative to pure

$FAPbI_3$ (*4*–*8*). The most successful recent strategies for stabilizing pure $FAPbI_3$ perovskite thin films still incorporate a small fraction of alloying cations, including incorporation of MA through use of methylammonium chloride (in conjunction with formamidinium formate) (*9*), methylammonium thiocyanate vapor (*10*), and methylammonium formate (*11*), or other cations, such as Cs^+ and methylenediammonium (*12*, *13*).

These approaches lead recent record efficiency tables, and power conversion efficiencies have now exceeded 25.5% in single junction and 29.5% in tandem configurations (*14*). Nonetheless, degradation to undesirable hexagonal by-products during the lifetime of a PV panel can still occur (*3*), especially in formulations that include MA cations. Nanoscale domains of hexagonal phase impurities can persist even in high-performing films that appear otherwise cubic in macroscopic measurements (*15*). These trace hexagonal domains induce clusters of deep trap states that are detrimental to performance (*16*, *17*), and seed photo-degradation under operational conditions (*15*). Eliminating these hexagonal phase impurities will be essential for commercial viability of these cells, but doing so requires a fundamental atomic-level understanding of why and how they form.

Improved cubic phase stability has been attributed to either tuning the Goldschmidt tolerance factor toward the perfect cubic perovskite structure through cation mixing (*7*, *18*), templating growth of the corner-sharing cubic structure (*10*, *11*), strain relaxation (*13*), or reducing intrinsic defect density (*9*). We show that stable, photoactive FA-rich perovskites exhibited small, symmetry breaking, octahedral tilting at room temperature and actually have a non-cubic structure. The magnitude of octahedral tilting is very small and only weak superstructure diffraction peaks are created that are below the noise threshold of traditional characterization techniques. We elucidated these features using local, low-dose, nanostructure

probes and sensitive photon counting detectors. This octahedral-tilt-stabilized (ots) phase is induced through the alloying of cations and acts as an inherent photoactive material stabilizer by frustrating the transformation from the photoactive noncubic phase to hexagonal wide-bandgap phases. Although this alloying approach provides apparent phase purity if viewed macroscopically, spatial heterogeneity in cation distribution in the film is associated with local nanoscopic regions that are not tilted and thus form residual hexagonal phase impurities (*15*, *17*). We demonstrate a strategy in which surface-bound ethylenediaminetetraacetic acid (EDTA) templated the growth of ots-$FAPbI_3$ throughout the bulk film, as elucidated by solid-state nuclear magnetic resonance (NMR) and nuclear quadrupole resonance (NQR) measurements. The ots-$FAPbI_3$ films showed exceptional stability against thermal, atmospheric, and light stressors without any cationic additives.

We first solution-processed thin films of triple-cation $Cs_{0.05}FA_{0.78}MA_{0.17}Pb(I_{0.83}Br_{0.17})_3$ perovskite on SiN transmission electron microscope (TEM) substrates following previously reported process (*16*). An electron diffraction (ED) pattern (maintaining low electron dose ~10 electrons/$Å^2$) extracted from a scanning ED (SED) measurement (*19*) of the film could in principle be indexed to a $[001]_c$ zone axis of the expected cubic perovskite *Pm-3m* structure with a lattice parameter of ~6.3 Å (Fig. 1A) (*7*, *16*). However, in these 5-nm spatial-resolution SED scans, extracted from individual grains 50 to 200 nm in size, very faint reflections, forbidden from appearing in the *Pm-3m* space group, were visible (white arrows in Fig 1A). The same forbidden reflections were also observed in measurements from many different sample batches and experimental measurements, as well as in analogous pure-iodide $Cs_{0.05}FA_{0.78}MA_{0.17}PbI_3$ thin films (Fig. S1). Thus, these triple-cation compositions, regardless of halide composition, have a non-cubic superstructure.

We attributed these superstructure reflections to octahedral tilting whereby the BX_6 corner sharing octahedra tilt away from perfect cubic symmetry into 1 of 15 lower symmetry space groups (Fig. S2) (*20*). We preclude that the superstructure reflections could be attributed to effects other than octahedral tilting, such as dynamical scattering, or cation ordering (see Supplementary Note 1). We also preclude that electron beam-induced structural changes affected the interpretation of our results as our measurements were acquired over an order of magnitude below the electron doses at which beam-induced effects are observed. We also observed these superstructure reflections in halide perovskite compositions known to possess a tilted, non-cubic, structure (*21*, *22*) (Fig. S3, see also (*19*) and Supplementary Note 1).

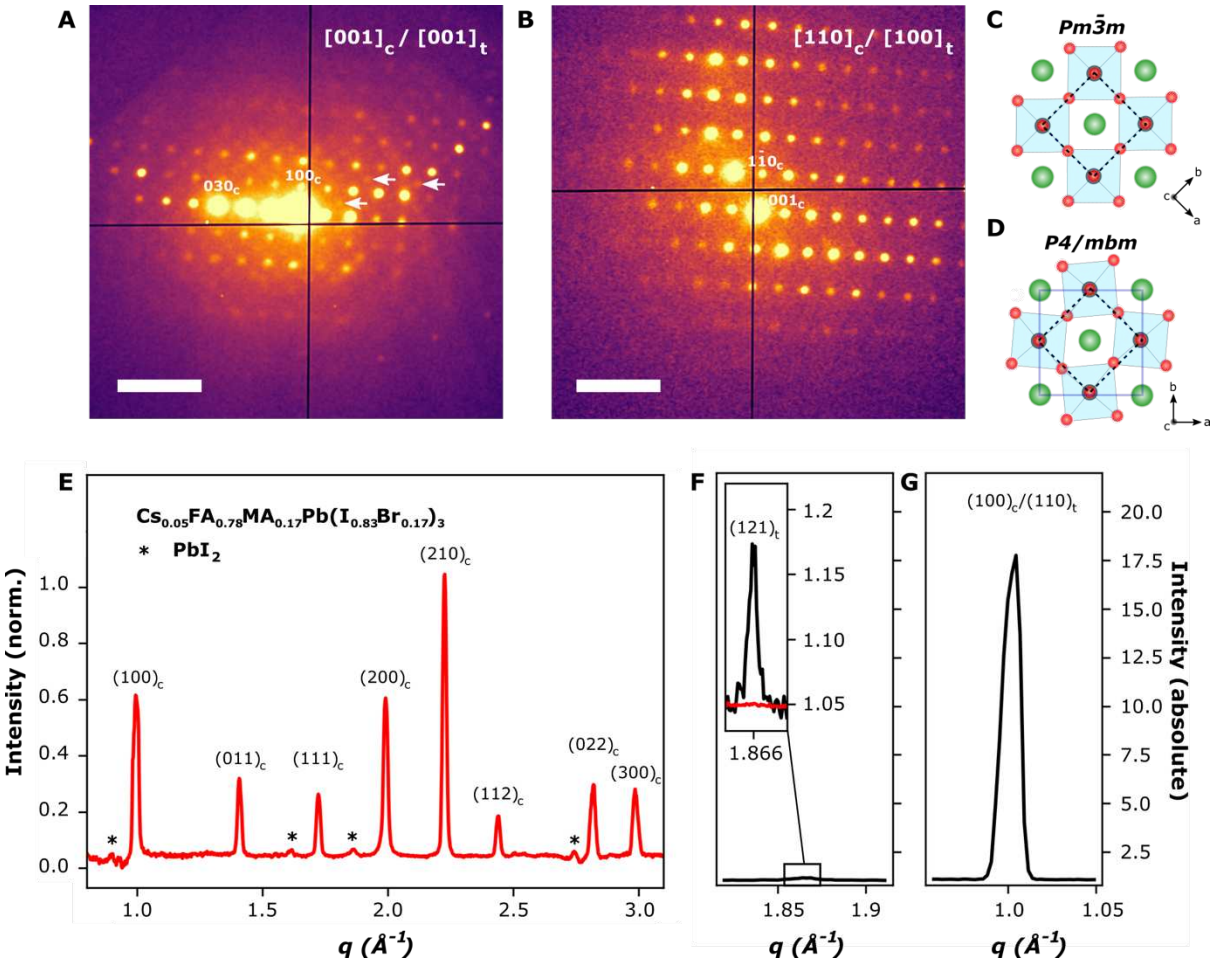

Fig. 1. Structural identification of tetragonal $Cs_{0.05}FA_{0.78}MA_{0.17}Pb(I_{0.83}Br_{0.17})_3$ thin films. **(A)** The ED pattern of a $Cs_{0.05}FA_{0.78}MA_{0.17}Pb(I_{0.83}Br_{0.17})_3$ sample oriented near the [001] zone

axis of a cubic unit cell ($[001]_c$) or the $[001]_t$ zone axis of a tetragonal unit cell. Superstructure reflections indicated by white arrows are forbidden from appearing in a cubic structure. **(B)** The ED pattern of a $Cs_{0.05}FA_{0.78}MA_{0.17}Pb(I_{0.83}Br_{0.17})_3$ film oriented near the $[110]_c$ / $[100]_t$ zone axis. Superstructure reflections are absent. **(C)** Schematic representation of the cubic *Pm-3m* perovskite structure viewed along the $[001]_c$ direction. Green spheres represent A-site cations and red spheres represent halides. B-site cations are represented by gray spheres that were partially visible and enclosed in blue octahedral cages. The cubic unit cell is indicated by a black dashed box. **(D)** Schematic representation of the tetragonal *P4/mbm* perovskite structure viewed along $[001]_c$. The tetragonal unit cell is indicated by the blue box connecting A-site cations. The pseudo-cubic unit cell is indicated by the black dashed box. **(E)** Mean nano x-ray-diffraction (nXRD) pattern of a $Cs_{0.05}FA_{0.78}MA_{0.17}Pb(I_{0.83}Br_{0.17})_3$ thin film extracted by spatially averaging across a (15 × 10) μm region. The pattern was normalized between 0 and 1 by subtracting the minimum value and scaling with the maximum value from the respective map of peak intensity ratio. **(F)** $(121)_t$ tetragonal XRD peak extracted from local nXRD measurements. Inset: zoom of $(121)_t$ peak (black) overlayed on the same region of *q*-space extracted from the mean nXRD scan (red), which shows no resolvable $(121)_t$ signal. **(G)** $(100)_c$/$(110)_t$ XRD peak extracted from local nXRD measurements. (F) and (G) are plotted on the same intensity scale. Scale bars in (A) and (B) are 0.5 $Å^{-1}$.

Interrogating superstructure reflections at particular orientations allows the unambiguous assignment of space groups from ED patterns of octahedrally tilted perovskites (*20*), and is typically achieved by tilting a single crystalline sample into different orientations and recording an ED pattern at each orientation. However, this methodology is not compatible with the most technologically relevant halide perovskite materials given their polycrystalline nature, small grains, and beam sensitivity. We used the low-dose, large-area scanning capabilities of SED to sample many individual grains at orientations other than $[001]_c$ and determine the actual symmetry of the FA-rich alloyed (triple-cation) perovskite unit cell.

Group-subgroup relations (Fig. S2), along with the symmetry of the experimentally observed superstructure reflections for triple-cation samples, indicated that the most likely space groups were either tetragonal *P4/mbm* or orthorhombic *Pnma* (*20*, *23*). However, the ED pattern of grains oriented near a $<110>_c$ zone axis (Fig. 1B and Fig. S4-S6) revealed no superstructure reflections when compared to the expected cubic structure. In the *Pnma* space group, superstructure reflections are expected in 2 of 12 $<110>_c$ zone axis diffraction patterns,

whereas in the *P4/mbm* space group, they are expected in none (Fig. S4) (*20*). The persistent absence of these reflections in our experimentally observed $<110>_c$ zone axis patterns thus provides strong evidence that these triple-cation perovskites had a tetragonal *P4/mbm* structure.

The weak nature of the superstructure reflections observed here, which were resolvable with SED given that the interaction of electrons with matter is orders of magnitude stronger than that of x-rays, suggested that the structural deviation from cubic (Fig. 1C, D) is very small and would be extremely difficult to detect in laboratory Bragg x-ray diffraction (XRD) (see (*19*)), and was consistent with previous assignments of the triple-cation perovskite to a cubic structure (*7*). We used synchrotron-based nano XRD (nXRD) experiments to quantify the degree of octahedral tilting present in FA-rich alloyed samples. A 50-nm focused x-ray probe allowed us to scan local regions of a sample, acquiring both single-crystal patterns from individual grains and powder patterns representative of the bulk of the material by spatially averaging across every probe position in a given scan. Even with monochromated synchrotron light and a highly sensitive photon counting detector (see (*19*)), we did not clearly observe tetragonal superstructure reflections in a spatially averaged nXRD pattern across a 15 μm × 10 μm region of a triple-cation film sample (Fig. 1E, and (*19*)) because the tetragonal superstructure peaks had an intensity below or comparable to the noise of the averaged pattern (Fig. 1F, inset shows no observable signal in average pattern).

However, the local nature of nXRD allowed us to use virtual dark-field imaging (Fig. S7, (*19*)) to exclusively extract regions in the scan where the Bragg condition was satisfied for tetragonal superstructure peaks. This approach substantially increased the signal-to-noise ratio and allowed extraction of local tetragonal superstructure peaks (Fig. 1F and inset). As the intensity of superstructure peaks relative to primary Bragg peaks was directly related to the

degree of octahedral tilting (*24*), we could compare the averaged intensities *I* of the tetragonal $(121)_t$ Bragg peak (Fig. 1F) to the much stronger primary $(100)_c/(110)_t$ Bragg peak (Fig. 1G) to show that $I_{(121)t}$ was 0.75% of $I_{(100)c/(110)t}$. A comparison of this relative intensity to kinematical simulations of a range of different octahedral tilt angles indicated an octahedral rotation in the range 0.75° to 2.75° about the c-axis of the unit cell (Fig. 1D) (see Fig. S7, (*19*) and Supplementary Note 2 for calculation of relative peak intensity, estimation of octahedral rotation and its range, and extraction of local diffraction data). Our collective results revealed that these FA-rich alloyed cation compositions intrinsically had small octahedral tilting structural distortions that were not observable in macroscopic Bragg diffraction experiments but resolvable by the local Bragg diffraction measurements employed here.

The crystallization of FA-rich alloyed perovskites in this slightly tilted corner sharing, photoactive phase at room temperature was surprising. We hypothesize that the ots phase led to reported improved stability and resistance to transforming into the hexagonal phases when compared to untreated cubic α-$FAPbI_3$ (*25*). To test whether the tilted octahedra of the tetragonal *P4/mbm* triple-cation perovskite provided an innate barrier to forming a hexagonal face-sharing structure, we probed the thermodynamics of the transformation between corner and face-sharing octahedral networks using first-principles density functional theory (DFT) total energy calculations (see (*19*)). We considered both the cubic *Pm-3m* phase (Fig. 2A) and the tetragonal *P4/mbm* (Fig. 2D) as the starting corner sharing phases and the same hexagonal *2H* phase as the final face-sharing phase (Fig. 2, C and F). The energy difference (thermodynamic driving force) between the cubic and hexagonal phases was 86 meV (Fig. 2G), whereas the difference between the tetragonal and hexagonal phase was only 17 meV.

We estimated the thermodynamic cost to form a mixed corner/face-sharing phase (Fig. 2B for cubic and 2E for tetragonal), which is an intermediate between the corner sharing and face sharing phases. These values provided a lower bound for the phase transition barrier: we obtain a barrier height of 26 meV/formula unit (f.u.) for the cubic-to-hexagonal phase transition and 75 meV/f.u. for the tetragonal-to-hexagonal phase transition, again indicating that the cubic phase was more susceptible to transitioning to hexagonal polytypes. We note that the phase transition may be further influenced by reorientations of the organic cation (*26*). Although transitions between cubic corner-sharing and hexagonal face-sharing structures are well documented in halide perovskites, oxide perovskites, and silicon carbide materials (*27–29*), the same is not true for tetragonal corner sharing (or other tilted structures) to hexagonal face sharing transitions.

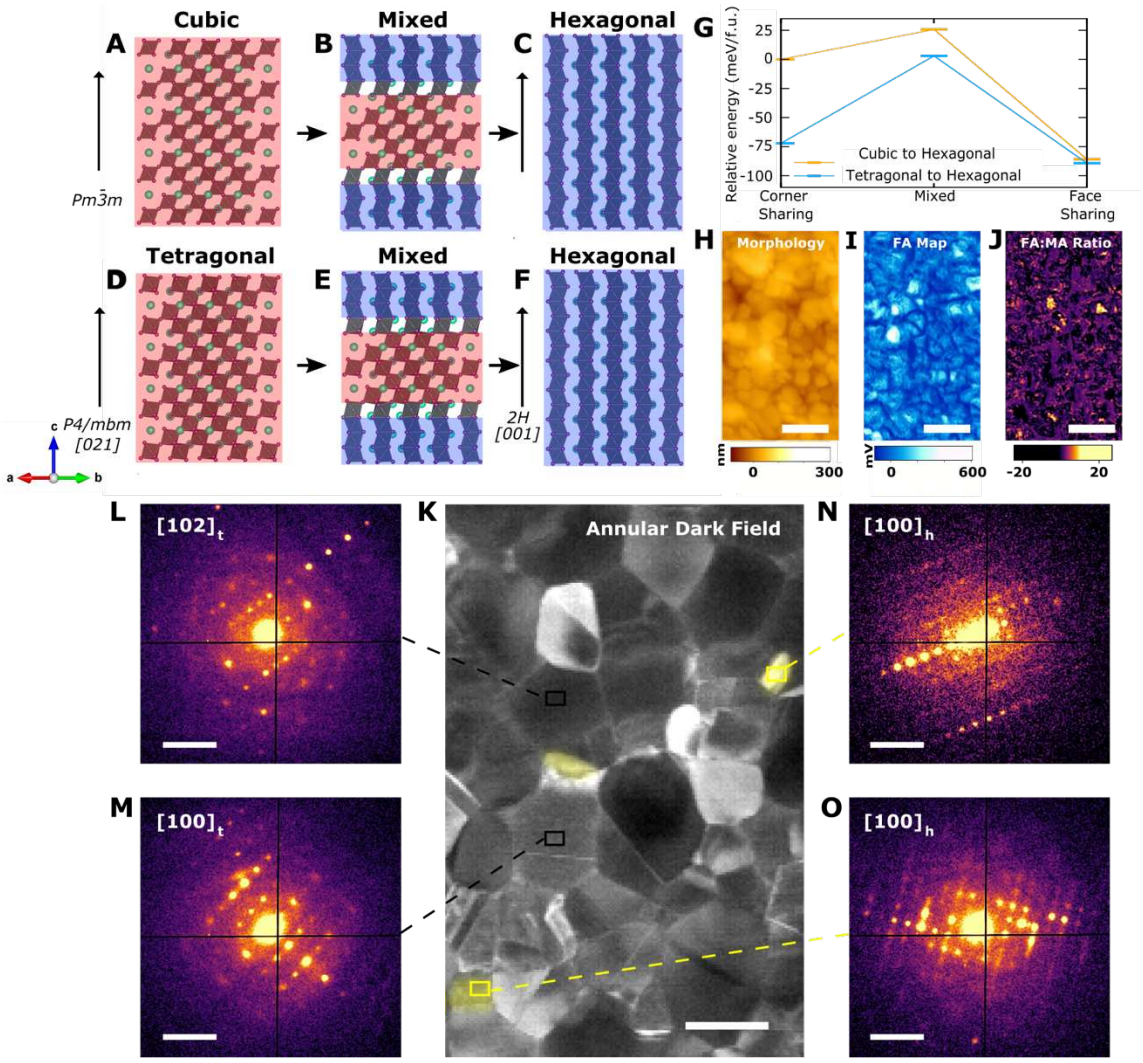

Fig. 2. Tilted octahedra stabilize photoactive perovskites against degradation. (A to C) Progression of the structural transition from **(A)** the corner-sharing cubic *Pm-3m* structure to **(C)** the *2H* hexagonal face-sharing structure by way of a **(B)** mixed corner-sharing and face sharing intermediary structure. **(D-F)** Progression of the structural transition from **(D)** the corner-sharing tetragonal *P4/mbm* structure to **(F)** the *2H* hexagonal face-sharing structure by way of a **(E)** mixed corner-sharing and face-sharing intermediate structure. **(G)** Relative energy difference between the corner-sharing, mixed, and face-sharing phases for the cubic-to-hexagonal (gold) and tetragonal-to-hexagonal (blue) transition. For a $Cs_{0.05}FA_{0.78}MA_{0.17}Pb(I_{0.83}Br_{0.17})$ thin film, **(H)** AFM-IR morphology map and **(I)** IR absorption maps of the FA content (peak at 1712 cm^{-1}) **(J) IR** chemical ratio of the FA:MA cation distribution extracted by dividing the IR map of FA content in I by the IR map of MA content in Fig. S8. **(K)** Annular dark field image reconstructed from SED data of a region of a $Cs_{0.05}FA_{0.78}MA_{0.17}Pb(I_{0.83}Br_{0.17})_3$ thin film. Hexagonal phase impurities are shaded in yellow. **(L and M)** ED patterns extracted from a black region of interest in K revealing (L) a grain oriented near the $[102]_t$ zone axis and (M) a grain oriented near the $[100]_t$ zone axis. **(N** and **O)** ED patterns of the yellow box region of interest shown in K revealing a *2H* hexagonal phase

impurity (N) oriented near the $[100]_h$ zone axis and (O) oriented near the $[100]_h$ zone axis. Scalebars are 800 nm (H),(I),(J), 200 nm in (K) and 0.5 $Å^{-1}$ in (L), (M), (N), (O).

Given we observed the tetragonal structure in both mixed halide and single halide FA-rich alloyed cation compositions (Fig. 1A, B; Fig. S1), and that the structurally similar α-$FAPbI_3$ had an average cubic structure at room temperature, as revealed by neutron diffraction experiments (*25*), we propose that room-temperature octahedral tilting in FA-rich perovskites originated primarily from alloying of the FA, Cs^+, or MA cations (or some combination) on the A-site. Specifically, the mixing of differently sized cations induced a small distortion of the perovskite's local unit cell that frustrated the structural transformation to *2H* and other hexagonal phases. We note that halide mixing could additionally influence the observed degree of octahedral tilting (Fig. S8, Supplementary Note 1) (*19*).

Using atomic force microscopy based infrared nanospectroscopy (AFM-IR) to simultaneously map the morphology of the film (Fig. 2H) and the spatial distribution of the chemical signature of the FA (at 1712 cm^{-1}, Fig. 2I) and MA (1466 cm^{-1}, Fig. S8) of a triple-cation perovskite thin film, we observed discrete FA-rich regions of the film ~50 to 200 nm in size, as seen in the FA:MA ratio map in Fig. 2J (see also Fig. S9) (*30*). SED measurements (Fig. 2K) revealed that although most of the film exhibited *P4/mbm* symmetry (Fig. 2, K to M), we also observed discrete inclusions indexable to hexagonal polytype structures ~50 to 150 nm in size and comparable to the length scales of the FA-rich domains (Fig. 2, K, N, and O; see Fig. S10 for additional examples).

Based on these observations, we concluded that these hexagonal regions were linked to the heterogeneity in the cation distribution. For example, regions of the film with a local excess of FA, such as those visualized by AFM-IR (Fig. 2, I and J), had a reduced content of Cs^+, MA,

or both (Fig. 2, J and K; Fig. S9). The locally higher FA content allowed hexagonal phases to form either directly during the crystallization process (which cation alloying would otherwise have inhibited) (*2*, *31*), or indirectly after annealing as the FA-rich environment favored the formation of the photoactive perovskite as a cubic *Pm-3m* structure rather than a tetragonal *P4/mbm* structure. The cubic structure then readily transformed to *2H* and other hexagonal phases.

Even if these phases appear stabilized when probed macroscopically through small additions of other cations (*2*, *32*), typically-used film-processing approaches for devices can leave phase impurities that persist on the nanoscale (in general unobservable in macroscopic techniques) (*16*, *17*) and seed degradation under operation (*15*). The pathway to highly stable and efficient FA-rich perovskite devices is through the slight distortion of octahedral cages across the sample to a degree that frustrates the transition from corner-sharing to face sharing structures but does not compromise optoelectronic properties, for example by widening the bandgap or reducing carrier lifetimes (*33*). To selectively induce octahedral tilt in $FAPbI_3$ at room temperature without alloying multiple A-site cations, we used ethylenediaminetetraacetic acid (EDTA) as an additive to the precursor solution of $FAPbI_3$ (see (*19*) and SM) considering the potential for such bifunctional molecules to interact with both Pb^{2+} ions and ammonium cations in precursor solutions, during film formation, or both. We spin coated EDTA-containing perovskite precursors on substrates that were then annealed at 150° C for 1 h in a nitrogen glove box to form a visibly stable, optically active black phase film (see Fig. S11 for optimization of EDTA concentration). We did not include any other additives, which allowed us to study the pure $FAPbI_3$ systems.

SED patterns extracted from the resulting perovskite thin films (Fig 3, A and B) confirmed the presence of superstructure reflections identical to those observed in the *P4/mbm* FA-rich perovskites, indicating octahedral tilting occurred in the fabricated $FAPbI_3$. Occasionally, superstructure reflections inconsistent with *P4/mbm* symmetry were observed (Fig. S12) suggesting that multiple octahedral tilt systems were present that we were unable to unambiguously assign. Notably, everywhere we observed a corner-sharing photoactive perovskite structure, we observe octahedral tilting in ots-$FAPbI_3$. Furthermore, in the infrequent local regions where octahedral tilting was not observed, hexagonal phase impurities were present (Fig. 3C). These results provided further support for our assertion that octahedral tilt is critical for minimizing the formation of such phase impurities.

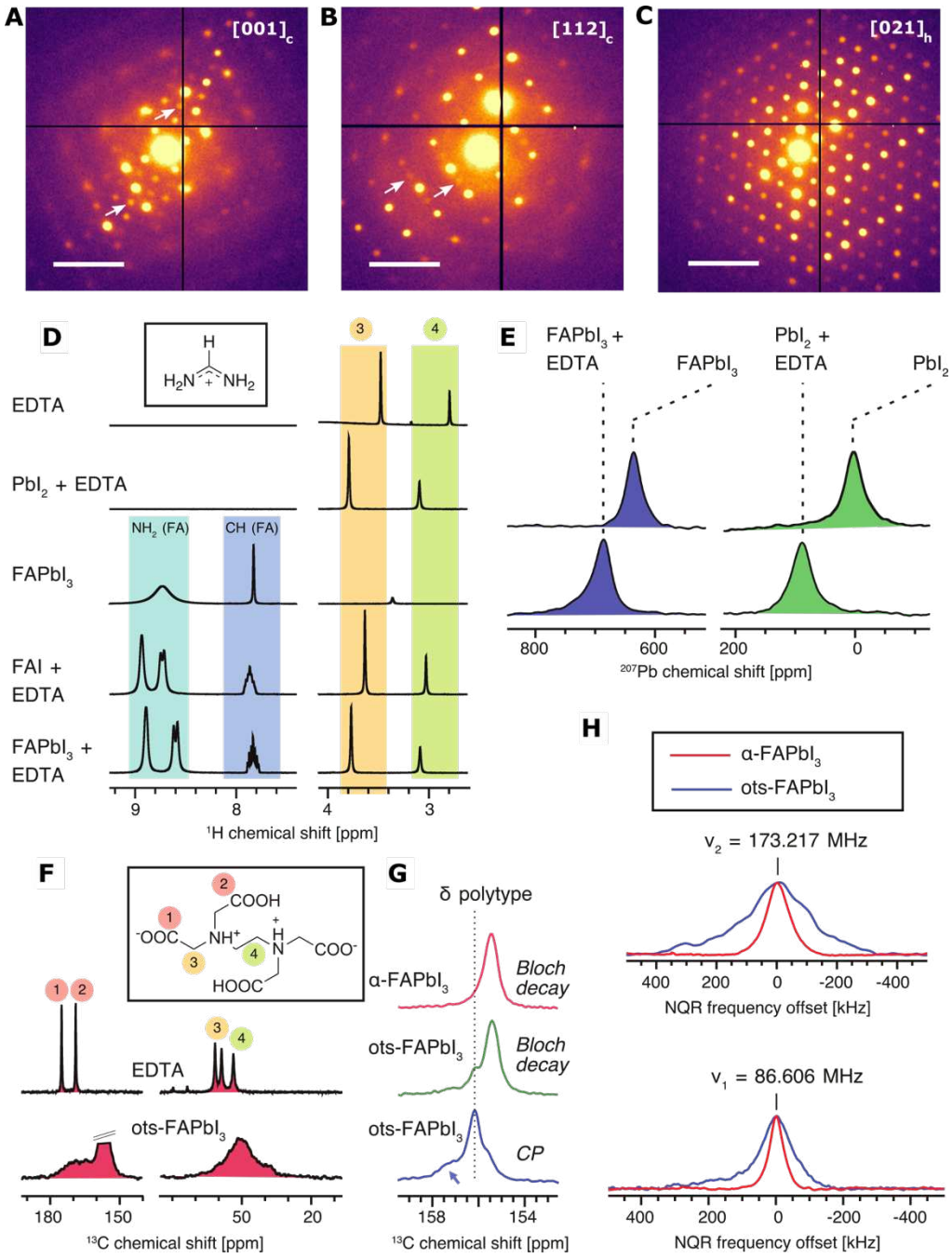

Fig. 3. Surface-bound ethylenediaminetetraacetic acid (EDTA) templates growth of octahedral-tilt-stabilised (ots) $FAPbI_3$. The SED pattern for ots-$FAPbI_3$ perovskite thin films near the (**A**) $[001]_c$ and **(B)** $[112]_c$ zone axes. A subset of superstructure reflections is highlighted with white arrows in each SED pattern. **(C)** The SED pattern for a hexagonal (6H) structure present in the ots-$FAPbI_3$ perovskite thin film oriented near the [021] zone axis. **(D)** Liquid-state ^1H NMR of the precursor solution reveals that EDTA interacts with Pb^{2+} and FA ions from PbI_2, FAI as well as $FAPbI_3$. The protonation of FA by EDTA hinders the rotation around the partial double C–N bonds rendering the two NH_2 moieties inequivalent (visible as the FA peak splitting). The inset shows the structure of protonated FA. (**E**) Liquid state ^{207}Pb NMR corroborates the Pb^{2+}-EDTA interaction in the precursor solution of dissolved PbI_2 and

$FAPbI_3$. (**F**) ^{1}H-^{13}C CP MAS NMR reveals that EDTA in EDTA-doped $FAPbI_3$ (scraped-off material from drop-cast films) is substantially disordered compared to neat EDTA. The intense peak of FA environments is clipped here for clarity. The inset shows the structure of EDTA. (**G**) The "FA" region of the Bloch-decay-detected (i.e., pulse-acquire) ^{13}C MAS NMR spectrum (green) shows that most of the FA environments are unchanged in ots-$FAPbI_3$ and correspond to FA within α-$FAPbI_3$. New environments are also present that correspond to δ-$FAPbI_3$ as well as FA interacting with EDTA (indicated by an arrow in the CP spectrum, blue). **(I)** ^{127}I nuclear quadrupole resonance (NQR) spectra of α-$FAPbI_3$ and ots-$FAPbI_3$ reveal more asymmetric local structure of iodides in the latter material. We attributed this effect to the overall crystallographic symmetry being reduced as a result of structure templating by the surface-bound EDTA. Scalebars in A, B, and C are 0.7 $Å^{-1}$.

To elucidate the microscopic mechanism of the EDTA-induced stabilization of $FAPbI_3$, we performed NMR experiments to probe local structure (*34*, *35*). ^{1}H liquid-state NMR of the precursor solutions showed a prominent shift of the acetate and ethylenic CH_2 groups of EDTA, added in the neat acid form (*36*), in the presence of dissolved PbI_2 at $\Delta\delta = +0.3$ parts per million (ppm) and $FAPbI_3$ at $\Delta\delta = +0.3$ ppm (Fig. 3D). Although EDTA is a strong chelator, we did not observe the formation of a long-lived, hexadentate Pb-EDTA chelate that would lead to splitting of the acetate methylene protons (see Supplementary Note 3) (*37*). We attributed the relative shifts to a combination of changes in the protonation equilibrium because EDTA can exist in six forms with different protonation levels, and a shorter-lived or more disordered Pb^{2+}-EDTA complex. Additional proof of the Pb^{2+}-EDTA interaction was provided by the relative shift in ^{207}Pb NMR spectra of the precursor solutions when EDTA is added (Fig. 3E). In addition, EDTA protonates the FA moiety, hindering the C–N bond rotation, as indicated by the appearance of a set of signals associated with the two inequivalent NH_2 groups of FA and the corresponding CH multiplet (*38*).

We next investigated ots-$FAPbI_3$ by solid-state NMR. ^{207}Pb and ^{14}N solid-state NMR spectra of scraped-off material from drop-cast films showed that the perovskite component of ots-$FAPbI_3$ was virtually identical to that of control α-$FAPbI_3$, within the sensitivity of these

two techniques (Fig. S13). ^{13}C Solid-state NMR allowed us to elucidate the speciation of EDTA in the ots-$FAPbI_3$ material (Fig. 3F). Although neat crystalline EDTA is characterized by narrow ^{13}C resonances (FWHM of 0.3-0.9 ppm), the FWHM of both the carbonyl and methylene carbons in ots-$FAPbI_3$ was 14 to 15 ppm, indicating that the EDTA was in an amorphous phase (or component). The ^{13}C resonances of FA revealed that there were multiple FA-containing local environments. Although the largest component corresponded to the three-dimensional perovskite phase of ots-$FAPbI_3$, there was also a smaller component corresponding to the residual δ-phase, consistent with the presence of small fractions of hexagonal polytypes in the SED data (Fig. 3C).

We also detected another substantially broader FA peak corresponding to a more disordered FA local environment, which we attribute to the interfacial FA ions of the perovskite phase interacting directly with EDTA (indicated by an arrow in Fig. 3G). Cross-polarization (CP) indicates that the local environment was rigid and not undergoing rapid near-isotropic reorientation characteristic for FA inside the A-site cation cage. ^{14}N NMR is highly sensitive to changes in lattice symmetry induced by incorporation of additives into the perovskite structure (*35*). The ^{14}N spectrum of the fast-reorienting FA inside a 3D perovskite cage (Fig. S13) showed that the symmetries of ots-$FAPbI_3$ and control α-$FAPbI_3$ are essentially identical within the sensitivity of this approach, indicating that the EDTA did not incorporate into the perovskite structure.

To elucidate the much smaller effect EDTA had on the lattice symmetry, we used ^{127}I nuclear quadrupole resonance (NQR). In NQR, the nuclear energy levels are split by the electric field gradient (EFG) around the nucleus and not by an external magnetic field, as in NMR (Fig. S13). The resulting transitions can be driven at specific frequencies that depend on

the magnitude of the EFG, which is determined by local symmetry. The NQR spectrum of the control α-$FAPbI_3$ sample contained two signals corresponding to the ±3/2↔±5/2 and ±1/2↔±3/2 transitions of the ^{127}I nucleus at 173.217 and 86.606 MHz, with FWHM of 87 and 47 kHz, respectively (Fig. 3H). The broadening of the ^{127}I NQR resonances in ots-$FAPbI_3$ (FWHM of 246 and 112 kHz for ±3/2↔±5/2 and ±1/2↔±3/2, respectively) evidenced that there was a broader distribution of local iodide environments compared to the control α-$FAPbI_3$. This result was consistent with the resulting octahedrally tilted phase having lower symmetry.

In a tetragonal $FAPbI_3$, each of the two NQR resonances present in cubic $FAPbI_3$ would split into two since there were two crystallographically inequivalent iodide sites in the unit cell of tetragonal $FAPbI_3$ (*39*). Splitting was not observed here indicating that the degree of distortion is characterized by a distribution rather than a clear-cut value throughout the material, consistent with SED observations of multiple local octahedral tilting symmetries (Fig. S12). The FWHM of the ±3/2↔±5/2 transition of ots-$FAPbI_3$ (246 kHz) corresponds to the maximum degree of distortion present in neat tetragonal β-$FAPbI_3$ at ca. 280 K (*40*). Notably, ^{14}N NMR (Fig. S13), which has recently been used to show that the symmetry of A-site cation cages of $FAPbI_3$ increases when it is stabilized with methylammonium thiocyanate (*10*), was not sensitive enough to detect the minor deviations from cubic symmetry identified here by NQR, SED and nXRD (Supplementary Note 4). Taken together, we induce octahedral distortion in the material through a structure-directing effect of EDTA, with the EDTA binding to the $FAPbI_3$ surface but not incorporating into the $FAPbI_3$ structure. We expect that this will spur further experimental and computational work to establish the exact binding modes of EDTA, identify other growth-templating additives, and understand their effect on crystallization and the resulting spatial variation of the tilt.

We examined octahedral tilt stabilization of the $FAPbI_3$ films by subjecting them to a variety of external stressors. The bulk XRD pattern of the ots-$FAPbI_3$ film (Fig. 4A, red) could in principle be indexed to a *Pm-3m* cubic structure, despite possessing a lower-symmetry tilted structure (cf. Fig. 3A, B), as the superstructure reflections arising from octahedral tilting were below the detection limit of bulk XRD measurements. There was no macroscopic evidence for phase impurities, despite trace amounts on the nanoscale (cf. Fig. 3C), consistent with the clean absorption and photoluminescence (PL) spectra observed (Fig. 4A, top inset). However, the control α-$FAPbI_3$ films showed the macroscopic presence of the *2H* δ-phase after only ~5 minutes (time required to load and measure the sample) of air exposure (XRD peak at 11.6º, Fig 4A, black), together with an asymmetric PL peak (Fig. 4A, inset; see Fig. S14 for cleaner PL spectra of encapsulated control samples). Furthermore, the PL lifetime of the control α-$FAPbI_3$ film was reduced by a factor of 4 with respect to an ots-$FAPbI_3$ film (Fig. S14), consistent with the phase impurities in the control films acting as non-radiative recombination centers (*17*). Exposure of the control film to ambient air for 3 hours caused the PL spectral shape and position to change rapidly and substantially (Fig. 4A, bottom inset). These changes were concomitant with further growth of the intensity of the *2H* δ-phase peak (Fig. S15).

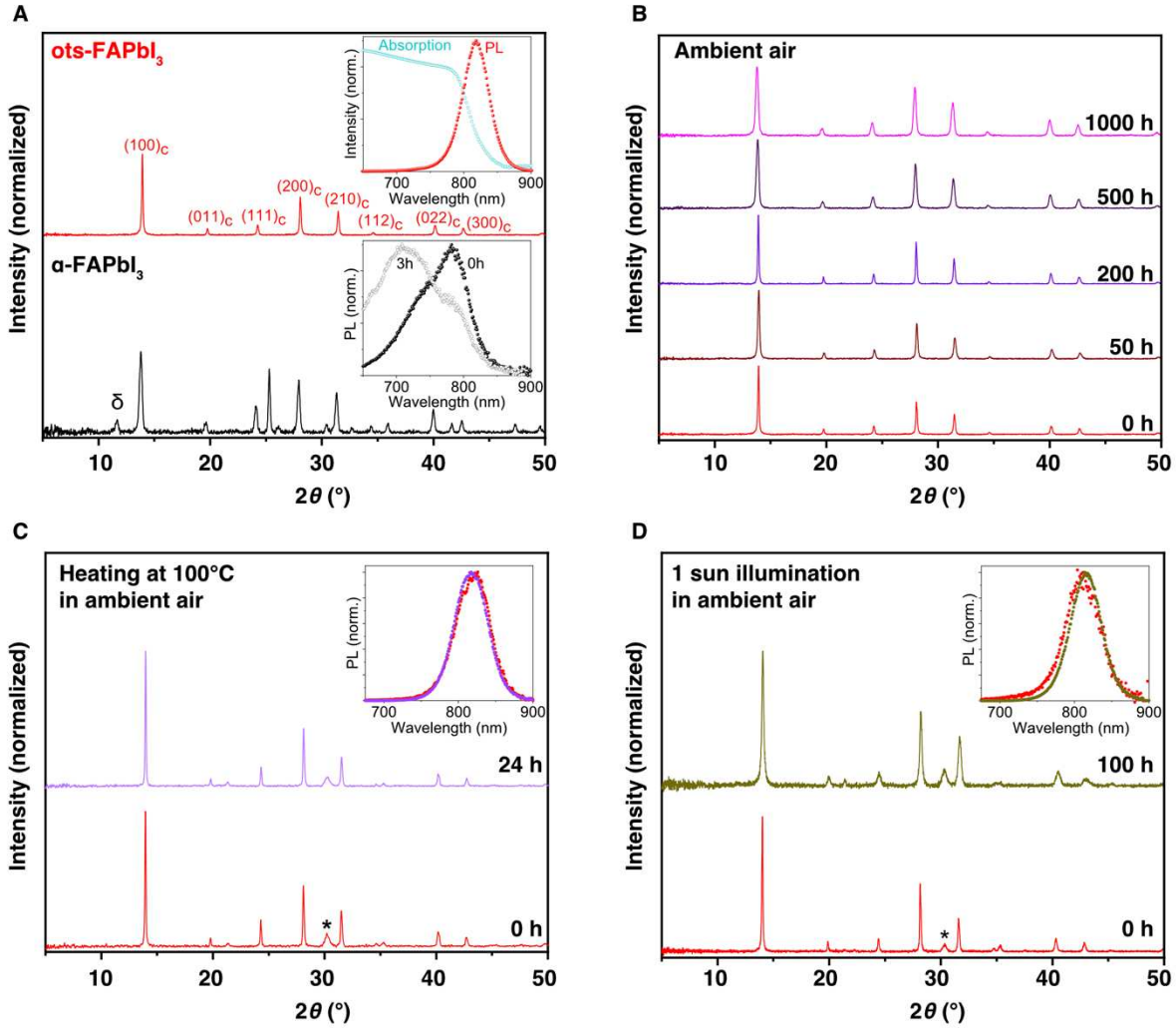

Fig. 4. Octahedral-tilt-stabilized (ots)-$FAPbI_3$ perovskite films are highly stable against atmospheric, thermal, and light stressors. (A) X-ray diffraction (XRD) pattern for a control α-$FAPbI_3$ sample (bottom pattern, black) taken immediately after exposing to ambient air, with a δ-phase peak already present. The inset shows PL spectra of a film taken initially (0 h corresponds to ~ 5 minutes of total exposure to ambient air) and again after 3 hours of exposure. We note these control α-$FAPbI_3$ films are rapidly degrading during the measurements in ambient air, and thus these spectra are merely snapshots in time of the samples during the degradation. The top pattern (red) shows the XRD pattern of an ots-$FAPbI_3$ film, indexed to the cubic structure for labelling purposes, with no signature of additional phase impurities. The inset shows the corresponding absorption (blue open symbols) and PL (red closed symbols) spectra of the film. **(B)** XRD pattern of an ots-$FAPbI_3$ film stored in ambient air over a period of 1000 hours, showing negligible change. **(C)** XRD pattern of an ots-$FAPbI_3$ film subjected to continuous heating at 100°C for 24 h in ambient air, showing very little change. The inset shows that the PL spectra also exhibit minimal change after the heating. **(D)** XRD pattern of an ots-$FAPbI_3$ film subjected to continuous illumination under 1 sun intensity (AM1.5) for 100 h in ambient air, showing only small changes in patterns. The inset shows that the PL spectra also exhibit minimal change after the illumination, other than a small spectral narrowing. * in C and D denotes peak from the ITO substrate.

After 1000 hours in ambient air, XRD patterns of the ots-$FAPbI_3$ films did not show any macroscopic conversion to hexagonal phases (Fig. 4B), and we only observed the presence of impurity phases after 1500 hours of air exposure (Fig. S16). Furthermore, we observe similar phase stability when heating the ots-$FAPbI_3$ perovskite films in ambient air for 24 hours at 100 °C, with negligible change in the XRD pattern (Fig. 4C; similar results in nitrogen, Fig. S17) or PL spectra (Fig. 4C, inset) after this extended heating. After continuous illumination of the ots-$FAPbI_3$ film under 1 sun (AM1.5) intensity for 100 hours in ambient air, there were no phase impurities evident in XRD (Fig. 4D) or sizable changes observed in PL spectra (Fig. 4D, inset) other than a slight narrowing of the peak and a very slight redshift, the origin of which is currently unclear. The PL properties of the ots-$FAPbI_3$ films were actually enhanced after the heating and illumination tests: the PL lifetimes reached 83 ns after the heating (Fig. S18) and 592 ns after the illumination (Fig. S19), consistent with light- and oxygen-assisted passivation reported previously for halide perovskites (*40*). These combined results show the resilient stabilizing effect against the generation of impurity phases that the octahedral tilting imparts on photoactive FA-rich perovskites, even for bare films in ambient air under rigorous external stressors.

We have shown that the intrinsic stabilization mechanism of FA-rich mixed-cation systems is an octahedral tilt induced by cation alloying. This octahedral tilting is so minor (~2°) as to be undetectable with bulk characterization techniques yet, remarkably, frustrates the transformation from photoactive, tilted perovskite phases to wide-bandgap, performance-limiting hexagonal polytypes (e.g. the *2H* δ-phase). We propose that the recent reports of stabilized cubic α-$FAPbI_3$ which have produced devices that are leading the efficiency tables and make use of both constituent cations and other additives to improve stability, inadvertently benefit from this same minor octahedral tilting (*9–13*). However, homogenously inducing a

tilted structure through cation alloying across a perovskite film is already challenging at lab-scale and will only become more so at commercial scale. Any local regions (even trace amounts) of a fabricated FA-rich perovskite that do not possess a tilted structure and are thus cubic will more readily transform to hexagonal phases, which generates non-absorbing material as well as deep traps and photo-degradation pathways under operation (*15*, *17*).

Developing new strategies that can work both in conjunction with cation alloying approaches, and independent of them, to homogenize nanoscale phase stability and eliminate residual traps will be critical to realize single-junction and tandem perovskite photovoltaics operating near their performance limits throughout their commercial life-cycle (*41*). This is especially true for the most promising compositions for single-junction commercialization such as α-$FAPbI_3$, where cationic additives produce unwanted shifts to higher bandgap and compromise thermal stability (*6*, *7*, *9*). Here, we have outlined key guidelines for achieving this, by templating growth of octahedral tilting through additives that do not incorporate into the perovskite structure, such as EDTA, without the use of additional A-site cations.

References and Notes

1. T. Chen, B. J. Foley, C. Park, C. M. Brown, L. W. Harriger, J. Lee, J. Ruff, M. Yoon, J. J. Choi, S.-H. Lee, Entropy-driven structural transition and kinetic trapping in formamidinium lead iodide perovskite. *Science Advances*. **2**, e1601650.

2. P. Gratia, I. Zimmermann, P. Schouwink, J.-H. Yum, J.-N. Audinot, K. Sivula, T. Wirtz, M. K. Nazeeruddin, The Many Faces of Mixed Ion Perovskites: Unraveling and Understanding the Crystallization Process. *ACS Energy Lett.* **2**, 2686–2693 (2017).

3. P. Ernesto Marchezi, E. Moreira Therézio, R. Szostak, H. Campos Loureiro, K. Bruening, A. Gold-Parker, M. A. Melo, C. J. Tassone, H. C. N. Tolentino, M. F. Toney, A. Flávia Nogueira, Degradation mechanisms in mixed-cation and mixed-halide Cs x FA 1−x Pb(Br y I 1−y) 3 perovskite films under ambient conditions. *Journal of Materials Chemistry A*. **8**, 9302–9312 (2020).

4. W. S. Yang, J. H. Noh, N. J. Jeon, Y. C. Kim, S. Ryu, J. Seo, S. I. Seok, High-performance photovoltaic perovskite layers fabricated through intramolecular exchange. *Science*. **348**, 1234–1237 (2015).

5. W. S. Yang, B.-W. Park, E. H. Jung, N. J. Jeon, Y. C. Kim, D. U. Lee, S. S. Shin, J. Seo, E. K. Kim, J. H. Noh, S. I. Seok, Iodide management in formamidinium-lead-halide–based perovskite layers for efficient solar cells. *Science*. **356**, 1376–1379 (2017).

6. N. J. Jeon, J. H. Noh, W. S. Yang, Y. C. Kim, S. Ryu, J. Seo, S. I. Seok, Compositional engineering of perovskite materials for high-performance solar cells. *Nature*. **517**, 476–480 (2015).

7. M. Saliba, T. Matsui, J.-Y. Seo, K. Domanski, J.-P. Correa-Baena, M. K. Nazeeruddin, S. M. Zakeeruddin, W. Tress, A. Abate, A. Hagfeldt, M. Grätzel, Cesium-containing triple cation perovskite solar cells: improved stability, reproducibility and high efficiency. *Energy Environ. Sci.* **9**, 1989–1997 (2016).

8. T. Bu, J. Li, H. Li, C. Tian, J. Su, G. Tong, L. K. Ono, C. Wang, Z. Lin, N. Chai, X.-L. Zhang, J. Chang, J. Lu, J. Zhong, W. Huang, Y. Qi, Y.-B. Cheng, F. Huang, Lead halide–templated crystallization of methylamine-free perovskite for efficient photovoltaic modules. *Science*. **372**, 1327–1332 (2021).

9. J. Jeong, M. Kim, J. Seo, H. Lu, P. Ahlawat, A. Mishra, Y. Yang, M. A. Hope, F. T. Eickemeyer, M. Kim, Y. J. Yoon, I. W. Choi, B. P. Darwich, S. J. Choi, Y. Jo, J. H. Lee, B. Walker, S. M. Zakeeruddin, L. Emsley, U. Rothlisberger, A. Hagfeldt, D. S. Kim, M. Grätzel, J. Y. Kim, Pseudo-halide anion engineering for α-FAPbI 3 perovskite solar cells. *Nature*. **592**, 381–385 (2021).

10. H. Lu, Y. Liu, P. Ahlawat, A. Mishra, W. R. Tress, F. T. Eickemeyer, Y. Yang, F. Fu, Z. Wang, C. E. Avalos, B. I. Carlsen, A. Agarwalla, X. Zhang, X. Li, Y. Zhan, S. M. Zakeeruddin, L. Emsley, U. Rothlisberger, L. Zheng, A. Hagfeldt, M. Grätzel, Vapor-assisted deposition of highly efficient, stable black-phase FAPbI3 perovskite solar cells. *Science*. **370** (2020), doi:10.1126/science.abb8985.

11. W. Hui, L. Chao, H. Lu, F. Xia, Q. Wei, Z. Su, T. Niu, L. Tao, B. Du, D. Li, Y. Wang, H. Dong, S. Zuo, B. Li, W. Shi, X. Ran, P. Li, H. Zhang, Z. Wu, C. Ran, L. Song, G. Xing, X. Gao, J. Zhang, Y. Xia, Y. Chen, W. Huang, Stabilizing black-phase formamidinium perovskite formation at room temperature and high humidity. *Science*. **371**, 1359–1364 (2021).

12. H. Min, M. Kim, S.-U. Lee, H. Kim, G. Kim, K. Choi, J. H. Lee, S. I. Seok, Efficient, stable solar cells by using inherent bandgap of α-phase formamidinium lead iodide. *Science*. **366**, 749–753 (2019).

13. G. Kim, H. Min, K. S. Lee, D. Y. Lee, S. M. Yoon, S. I. Seok, Impact of strain relaxation on performance of α-formamidinium lead iodide perovskite solar cells. *Science*. **370**, 108–112 (2020).

14. NREL, Best Research-Cell Efficiency Chart | Photovoltaic Research | NREL (2021), (available at https://www.nrel.gov/pv/cell-efficiency.html).

15. S. Macpherson, T. A. S. Doherty, A. J. Winchester, S. Kosar, D. N. Johnstone, Y.-H. Chiang, K. Galkowski, M. Anaya, K. Frohna, A. N. Iqbal, B. Roose, Z. Andaji-Garmaroudi, P. A. Midgley, K. M. Dani, S. D. Stranks, Local Nanoscale Defective Phase Impurities Are the Sites of Degradation in Halide Perovskite Devices. *arXiv:2107.09549 [cond-mat, physics:physics]* (2021) (available at http://arxiv.org/abs/2107.09549).

16. T. A. S. Doherty, A. J. Winchester, S. Macpherson, D. N. Johnstone, V. Pareek, E. M. Tennyson, S. Kosar, F. U. Kosasih, M. Anaya, M. Abdi-Jalebi, Z. Andaji-Garmaroudi, E. L. Wong, J. Madéo, Y.-H. Chiang, J.-S. Park, Y.-K. Jung, C. E. Petoukhoff, G. Divitini, M. K. L. Man, C. Ducati, A. Walsh, P. A. Midgley, K. M. Dani, S. D. Stranks, Performance-limiting nanoscale trap clusters at grain junctions in halide perovskites. *Nature*. **580**, 360–366 (2020).

17. S. Kosar, A. J. Winchester, T. A. S. Doherty, S. Macpherson, C. Petoukhoff, K. Frohna, M. Anaya, N. Chan, J. Madéo, M. K. L. Man, S. D. Stranks, K. M. Dani, Unraveling the varied nature and roles of defects in hybrid halide perovskites with time resolved photoemission electron microscopy. *Energy & Environmental Science* (In Press).

18. J. Y. Kim, J.-W. Lee, H. S. Jung, H. Shin, N.-G. Park, High-Efficiency Perovskite Solar Cells. *Chem. Rev.* **120**, 7867–7918 (2020).

19. Materials and methods are available as supplementary materials at the Science website.

20. D. I. Woodward, I. M. Reaney, Electron diffraction of tilted perovskites. *Acta Crystallogr B*. **61**, 387–399 (2005).

21. R. E. Beal, N. Z. Hagström, J. Barrier, A. Gold-Parker, R. Prasanna, K. A. Bush, D. Passarello, L. T. Schelhas, K. Brüning, C. J. Tassone, H.-G. Steinrück, M. D. McGehee, M. F. Toney, A. F. Nogueira, Structural Origins of Light-Induced Phase Segregation in Organic-Inorganic Halide Perovskite Photovoltaic Materials. *Matter*. **2**, 207–219 (2020).

22. S. Chen, X. Zhang, J. Zhao, Y. Zhang, G. Kong, Q. Li, N. Li, Y. Yu, N. Xu, J. Zhang, K. Liu, Q. Zhao, J. Cao, J. Feng, X. Li, J. Qi, D. Yu, J. Li, P. Gao, Atomic scale insights into structure instability and decomposition pathway of methylammonium lead iodide perovskite. *Nature Communications*. **9**, 4807 (2018).

23. R. dos Reis, H. Yang, C. Ophus, P. Ercius, G. Bizarri, D. Perrodin, T. Shalapska, E. Bourret, J. Ciston, U. Dahmen, Determination of the structural phase and octahedral rotation angle in halide perovskites. *Appl. Phys. Lett.* **112**, 071901 (2018).

24. G. O. Jones, P. A. Thomas, Investigation of the structure and phase transitions in the novel A-site substituted distorted perovskite compound Na0.5Bi0.5TiO3. *Acta Crystallographica Section B*. **58**, 168–178 (2002).

25. M. T. Weller, O. J. Weber, J. M. Frost, A. Walsh, Cubic Perovskite Structure of Black Formamidinium Lead Iodide, α-[HC(NH $_2$) $_2$]PbI $_3$, at 298 K. *J. Phys. Chem. Lett.* **6**, 3209–3212 (2015).

26. E. M. Mozur, A. E. Maughan, Y. Cheng, A. Huq, N. Jalarvo, L. L. Daemen, J. R. Neilson, Orientational Glass Formation in Substituted Hybrid Perovskites. *Chem. Mater.* **29**, 10168–10177 (2017).

27. L. S. Ramsdell, Studies on silicon carbide. *American Mineralogist*. **32**, 64–82 (1947).

28. C. C. Stoumpos, C. D. Malliakas, M. G. Kanatzidis, Semiconducting Tin and Lead Iodide Perovskites with Organic Cations: Phase Transitions, High Mobilities, and Near-Infrared Photoluminescent Properties. *Inorg. Chem.* **52**, 9019–9038 (2013).

29. S. Fop, K. S. McCombie, E. J. Wildman, J. M. S. Skakle, J. T. S. Irvine, P. A. Connor, C. Savaniu, C. Ritter, A. C. Mclaughlin, High oxide ion and proton conductivity in a disordered hexagonal perovskite. *Nat. Mater.* **19**, 752–757 (2020).

30. R. Szostak, J. C. Silva, S.-H. Turren-Cruz, M. M. Soares, R. O. Freitas, A. Hagfeldt, H. C. N. Tolentino, A. F. Nogueira, Nanoscale mapping of chemical composition in organic-inorganic hybrid perovskite films. *Science Advances*. **5**, eaaw6619 (2019).

31. H. T. Pham, Y. Yin, G. Andersson, K. J. Weber, T. Duong, J. Wong-Leung, Unraveling the influence of CsCl/MACl on the formation of nanotwins, stacking faults and cubic supercell structure in FA-based perovskite solar cells. *Nano Energy*. **87**, 106226 (2021).

32. H. X. Dang, K. Wang, M. Ghasemi, M.-C. Tang, M. De Bastiani, E. Aydin, E. Dauzon, D. Barrit, J. Peng, D.-M. Smilgies, S. De Wolf, A. Amassian, Multi-cation Synergy Suppresses Phase Segregation in Mixed-Halide Perovskites. *Joule*. **3**, 1746–1764 (2019).

33. R. Prasanna, A. Gold-Parker, T. Leijtens, B. Conings, A. Babayigit, H.-G. Boyen, M. F. Toney, M. D. McGehee, Band Gap Tuning via Lattice Contraction and Octahedral Tilting in Perovskite Materials for Photovoltaics. *Journal of the American Chemical Society*. **139**, 11117–11124 (2017).

34. L. Piveteau, V. Morad, M. V. Kovalenko, Solid-state NMR and NQR Spectroscopy of Lead-Halide Perovskite Materials. *J. Am. Chem. Soc.* (2020), doi:10.1021/jacs.0c07338.

35. D. J. Kubicki, S. D. Stranks, C. P. Grey, L. Emsley, NMR spectroscopy probes microstructure, dynamics and doping of metal halide perovskites. *Nat Rev Chem*. **5**, 624–645 (2021).

36. S. Aime, R. Gobetto, R. Nano, E. Santucci, 13C solid state CP/MAS NMR studies of EDTA complexes. *Inorganica Chimica Acta*. **129**, L23–L25 (1987).

37. E. Hafer, U. Holzgrabe, K. Kraus, K. Adams, J. M. Hook, B. Diehl, Qualitative and quantitative ^{1} H NMR spectroscopy for determination of divalent metal cation

concentration in model salt solutions, food supplements, and pharmaceutical products by using EDTA as chelating agent. *Magn Reson Chem*. **58**, 653–665 (2020).

38. W. T. M. Van Gompel, R. Herckens, G. Reekmans, B. Ruttens, J. D'Haen, P. Adriaensens, L. Lutsen, D. Vanderzande, Degradation of the Formamidinium Cation and the Quantification of the Formamidinium–Methylammonium Ratio in Lead Iodide Hybrid Perovskites by Nuclear Magnetic Resonance Spectroscopy. *J. Phys. Chem. C*. **122**, 4117–4124 (2018).

39. K. Yamada, S. Hino, S. Hirose, Y. Yamane, I. Turkevych, T. Urano, H. Tomiyasu, H. Yamagishi, S. Aramaki, Static and Dynamic Structures of Perovskite Halides ABX3 (B = Pb, Sn) and Their Characteristic Semiconducting Properties by a Hückel Analytical Calculation. *BCSJ*. **91**, 1196–1204 (2018).

40. R. Brenes, D. Guo, A. Osherov, N. K. Noel, C. Eames, E. M. Hutter, S. K. Pathak, F. Niroui, R. H. Friend, M. S. Islam, H. J. Snaith, V. Bulović, T. J. Savenije, S. D. Stranks, Metal Halide Perovskite Polycrystalline Films Exhibiting Properties of Single Crystals. *Joule*. **1**, 155–167 (2017).

41. Y. Deng, S. Xu, S. Chen, X. Xiao, J. Zhao, J. Huang, Defect compensation in formamidinium–caesium perovskites for highly efficient solar mini-modules with improved photostability. *Nat Energy*. **6**, 633–641 (2021).

42. A. Babayigit, J. D'Haen, H.-G. Boyen, B. Conings, Gas Quenching for Perovskite Thin Film Deposition. *Joule*. **2**, 1205–1209 (2018).

43. D. Prochowicz, M. Franckevičius, A. M. Cieślak, S. M. Zakeeruddin, M. Grätzel, J. Lewiński, Mechanosynthesis of the hybrid perovskite CH3NH3PbI3: characterization and the corresponding solar cell efficiency. *J. Mater. Chem. A*. **3**, 20772–20777 (2015).

44. D. Prochowicz, P. Yadav, M. Saliba, M. Saski, S. M. Zakeeruddin, J. Lewiński, M. Grätzel, Mechanosynthesis of pure phase mixed-cation MAxFA1−xPbI3 hybrid perovskites: photovoltaic performance and electrochemical properties. *Sustainable Energy Fuels*. **1**, 689–693 (2017).

45. M. U. Rothmann, J. S. Kim, J. Borchert, K. B. Lohmann, C. M. O'Leary, A. A. Sheader, L. Clark, H. J. Snaith, M. B. Johnston, P. D. Nellist, L. M. Herz, Atomic-scale microstructure of metal halide perovskite. *Science*. **370**, eabb5940 (2020).

46. Duncan N. Johnstone, Phillip Crout, Joonatan Laulainen, Simon Høgås, Ben Martineau, Tina Bergh, Stef Smeets, Sean Collins, Jędrzej Morzy, Håkon Ånes, Eric Prestat, Tiarnan Doherty, Tomas Ostasevicius, Mohsen Danaie, Rob Tovey, *pyxem/pyxem: pyxem 0.10.0* (Zenodo, 2019; https://zenodo.org/record/3533653#.XnIqC6j7SUk).

47. P. D. Quinn, L. Alianelli, M. Gomez-Gonzalez, D. Mahoney, F. Cacho-Nerin, A. Peach, J. E. Parker, The Hard X-ray Nanoprobe beamline at Diamond Light Source. *J Synchrotron Radiat*. **28**, 1006–1013 (2021).

48. Francisco de la Peña, Vidar Tonaas Fauske, Pierre Burdet, Eric Prestat, Petras Jokubauskas, Magnus Nord, Tomas Ostasevicius, Katherine E. MacArthur, Mike Sarahan, Duncan N. Johnstone, Joshua Taillon, Alberto Eljarrat, Vadim Migunov, Jan Caron, Tom Furnival, Stefano Mazzucco, Thomas Aarholt, Michael Walls, Tom Slater, Florian Winkler, Ben Martineau, Gaël Donval, Robert McLeod, Eric R. Hoglund, Ivo Alxneit, Ida Hjorth, Trond Henninen, Luiz Fernando Zagonel, Andreas Garmannslund, Alexander Skorikov, *hyperspy/hyperspy v1.4.1* (Zenodo, 2018; https://zenodo.org/record/1469364#.XKcr9OtKiRs).

49. G. Kresse, J. Furthmüller, Efficient iterative schemes for *ab initio* total-energy calculations using a plane-wave basis set. *Phys. Rev. B*. **54**, 11169–11186 (1996).

50. G. Kresse, J. Furthmüller, Efficiency of ab-initio total energy calculations for metals and semiconductors using a plane-wave basis set. *Computational Materials Science*. **6**, 15–50 (1996).

51. G. Kresse, D. Joubert, From ultrasoft pseudopotentials to the projector augmented-wave method. *Phys. Rev. B*. **59**, 1758–1775 (1999).

52. P. E. Blöchl, Projector augmented-wave method. *Phys. Rev. B*. **50**, 17953–17979 (1994).

53. J. P. Perdew, A. Ruzsinszky, G. I. Csonka, O. A. Vydrov, G. E. Scuseria, L. A. Constantin, X. Zhou, K. Burke, Restoring the Density-Gradient Expansion for Exchange in Solids and Surfaces. *Phys. Rev. Lett.* **100**, 136406 (2008).

54. C. R. Morcombe, K. W. Zilm, Chemical shift referencing in MAS solid state NMR. *Journal of Magnetic Resonance*. **162**, 479–486 (2003).

55. F. S. Ruggeri, B. Mannini, R. Schmid, M. Vendruscolo, T. P. J. Knowles, Single molecule secondary structure determination of proteins through infrared absorption nanospectroscopy. *Nat Commun*. **11**, 2945 (2020).

56. F. S. Ruggeri, J. Habchi, S. Chia, R. I. Horne, M. Vendruscolo, T. P. J. Knowles, Infrared nanospectroscopy reveals the molecular interaction fingerprint of an aggregation inhibitor with single Aβ42 oligomers. *Nat Commun*. **12**, 688 (2021).

57. A. N. Beecher, O. E. Semonin, J. M. Skelton, J. M. Frost, M. W. Terban, H. Zhai, A. Alatas, J. S. Owen, A. Walsh, S. J. L. Billinge, Direct Observation of Dynamic Symmetry Breaking above Room Temperature in Methylammonium Lead Iodide Perovskite. *ACS Energy Lett.* **1**, 880–887 (2016).

58. A. Oberlin, *Electron microscopy of thin crystals* by P. B. Hirsch, A. Howie, R. B. Nicholson, D. W. Pashley and M. J. Whelan. *Acta Cryst*. **21**, 454–454 (1966).

59. G. King, P. M. Woodward, Cation ordering in perovskites. *J. Mater. Chem.* **20**, 5785 (2010).

60. K. Kishida, K. Goto, H. Inui, Electron diffraction of ABX_3 perovskites with both layered ordering of *A* cations and tilting of BX_6 octahedra. *Acta Crystallogr B Struct Sci*. **65**, 405–415 (2009).

61. A. Franz, D. M. Többens, F. Lehmann, M. Kärgell, S. Schorr, The influence of deuteration on the crystal structure of hybrid halide perovskites: a temperature-dependent neutron diffraction study of FAPbBr3. *Acta Cryst B*. **76**, 267–274 (2020).

62. A. M. Askar, A. Karmakar, G. M. Bernard, M. Ha, V. V. Terskikh, B. D. Wiltshire, S. Patel, J. Fleet, K. Shankar, V. K. Michaelis, Composition-Tunable Formamidinium Lead Mixed Halide Perovskites via Solvent-Free Mechanochemical Synthesis: Decoding the Pb Environments Using Solid-State NMR Spectroscopy. *J. Phys. Chem. Lett.* **9**, 2671–2677 (2018).

63. C. Hammond, *The basics of crystallography and diffraction* (Oxford University Press, Oxford, Fourth edition., 2015), *International Union of Crystallography texts on crystallography*.

64. P. Crout, D. N. Johnstone, S. Høgås, B. Martineau, isabelwood100, J. Laulainen, H. W. Ånes, N. Cautaerts, S. Collins, S. Smeets, E. Jacobsen, J. Morzy, E. Prestat, phillipcrout, T. Doherty, AgBorrelli, T. Ostasevicius, R. Tovey, EirikOpheim, T. Bergh, *pyxem/diffsims: diffsims 0.4.2* (Zenodo, 2021; https://zenodo.org/record/4697299).

Acknowledgments:

The authors acknowledge Julia Parker and Paul Quinn for support during experiments on the I14 beamline at Diamond Light Source. **Funding:** T.A.S.D. acknowledges the support of a National University of Ireland Travelling Studentship. S.N. acknowledges the Royal Society and SERB for funding a Newton International Fellowship. S.D.S. acknowledges the Royal Society and Tata Group (UF150033). P.A.M. thanks the EPSRC for financial support under grant no. EP/R008779/1. The work has received funding from the European Research Council under the European Union's Horizon 2020 research and innovation programme (HYPERION - grant agreement no. 756962). The authors acknowledge the EPSRC (EP/R023980/1) for funding. K.F. acknowledges a George and Lilian Schiff Studentship, Winton Studentship, the Engineering and Physical Sciences Research Council (EPSRC) studentship, Cambridge Trust Scholarship, and Robert Gardiner Scholarship. D.J.K., E.M.T., and M.A. acknowledge funding from the Marie Skłodowska-Curie actions (grant agreements Nos. 841136, 841265, and 841386, respectively) under the European Union's Horizon 2020 research and innovation programme. A.N.I. acknowledges scholarships from the British Spanish Society and the Sir Richard Stapley Educational Trust. S.M. acknowledges funding from an Engineering and Physical Sciences Research Council (EPSRC) studentship. A.A. acknowledges funding from the Royal Society. S.M.C acknowledges support from a University Academic Fellowship at the University of Leeds. P.C. received funding from an Engineering and Physical Sciences Research Council (EPSRC) studentship. C.P.G thanks the EU ERC for an Advanced Fellowship DLV-835073. This work was also supported by a National Research Foundation of Korea grant (No. 2018R1C1B6008728). The work has received funding from the European Union's Horizon 2020. INFRAIA programme (ESTEEM3 - grant agreement no. 823717). The

authors thank Diamond Light Source for access and support in use of beamline I14 (proposal number sp20420) and the electron Physical Science Imaging Centre (Instrument E02 and proposal number MG24111) that contributed to the results presented here. Via our membership of the UK's HEC Materials Chemistry Consortium, which is funded by EPSRC (EP/L000202), this work used the ARCHER UK National Supercomputing Service (http://www.archer.ac.uk).
Authors Contributions: Conceptualization: TASD, SN, SDS. Methodology: TASD, SN, DJK, DNJ, CPG, AW, PAM, SDS. Investigation: TASD, SN, DJK, Y-KJ, DNJ, KF, FSR, DG, ANI, EMT, Y-HC, PC, MA, SM, MD, SMC, AA. Visualization: TASD, SN, DJK, SDS. Funding acquisition: SDS, AW, CPG, PAM. Project administration: SDS. Supervision: SDS, AW, CPG, PAM. Writing – original draft: TASD, SN, DJK, SDS. Writing – review & editing: TASD, SN, DJK, Y-KJ, DNJ, KF, FSR, DG, ANI, EMT, Y-HC, PC, MA, SM, AA, MD, SMC, CPG, AW, PM, SDS**. Competing Interests:** SDS is a co-founder of Swift Solar, Inc. **Data and materials availability:** The data that support the findings of this study are available from the corresponding author upon request and at the Apollo repository (*DOI to be added*). All (other) data needed to evaluate the conclusions in the paper are present in the paper or the Supplementary Materials.

Supplementary Materials

Materials and Methods

Supplementary Text

Figs. S1 to S19

Tables S1

References (*42* - *64*)

Science
AAAS

Supplementary Materials for

Title: Stabilized tilted-octahedra halide perovskites inhibit local formation of performance-limiting phases

Authors:
Tiarnan A.S. Doherty[1†], Satyawan Nagane[1†], Dominik J. Kubicki[1,2], Young-Kwang Jung[3], Duncan N. Johnstone[4], Affan N. Iqbal[1,5], Dengyang Guo[1,5], Kyle Frohna[1], Mohsen Danaie[6,7], Elizabeth M. Tennyson[1], Stuart Macpherson[1], Anna Abfalterer[1], Miguel Anaya[1,5], Yu-Hsien Chiang[1], Phillip Crout[4], Francesco Simone Ruggeri[8], Sean Collins[9], Clare P. Grey[2], Aron Walsh[3,10], Paul A. Midgley[4], Samuel D. Stranks[1,5*]

Affiliations:
[1]Department of Physics, Cavendish Laboratory, University of Cambridge; Cambridge, UK

[2]Yusuf Hamied Department of Chemistry, University of Cambridge; Lensfield Road, Cambridge, UK

[3]Department of Materials Science and Engineering, Yonsei University; Seoul, Korea

[4]Department of Materials Science and Metallurgy, University of Cambridge; Cambridge, UK

[5]Department of Chemical Engineering and Biotechnology, University of Cambridge; Cambridge, UK

[6]Electron Physical Science Imaging Centre, Diamond Light Source Ltd; Didcot, UK

[7]Department of Materials, University of Oxford; Oxford, UK

[8]Laboratory of Organic and Physical Chemistry, Wageningen University and Research, the Netherlands

[9]School of Chemical and Process Engineering & School of Chemistry, University of Leeds; Leeds, UK

[10]Department of Materials, Imperial College London; London, UK

† These authors contributed equally.

*sds65@cam.ac.uk

This PDF file includes:

Materials and Methods

Supplementary Text

Figs. S1 to S19

Table S1

Materials and Methods

Materials

N, N-Dimethylformamide (DMF, anhydrous, 99.8%), dimethyl sulfoxide (DMSO, anhydrous, 99.9%), isopropanol (anhydrous, 99.9%); Ethylenediaminetetraacetic acid (EDTA, anhydrous, ≥ 99%), chlorobenzene (CB, 99.99%) and cesium iodide (CsI, 99.999%, perovskite grade) were purchased from Sigma-Aldrich and used without further purification. Formamidinium iodide (FAI, 99.9%), methylammonium iodide (MAI, 99.9%) and methylammonium bromide (MABr, 99.9%) were purchased from Greatcell Solar Materials and used without further purification. Lead iodide (PbI_2, 98%) and lead bromide ($PbBr_2$, 98%) were purchased from TCI and used without further purification.

Synthesis of Materials

All perovskite films were prepared in a N_2-filled glove box. $(Cs_{0.05}FA_{0.78}MA_{0.17})Pb(I_{0.83}Br_{0.17})_3$ thin films were prepared from solutions containing FAI (1 M), MABr (0.2 M) PbI_2 (1.1 M), $PbBr_2$ (0.22 M) dissolved in anhydrous DMF:DMSO 4:1 (v:v). CsI dissolved in DMSO (1.5 M) was then added to the precursor solution. $(Cs_{0.05}FA_{0.78}MA_{0.17})PbI_3$ thin films were prepared from precursor solutions containing FAI (1 M), PbI_2 (1.32 M), and MAI (0.2 M) in anhydrous DMF:DMSO 4:1 (v:v). CsI dissolved in DMSO (1.5 M) was then added to the precursor solution. For preparation on TEM grids, the precursor solution was diluted one part precursor solution to two parts solvent mixture (DMF and DMSO 4:1 v:v) resulting in a film thickness of ~ 200 nm. SiN windows from Norcada (part number: NT025X) were used as TEM grids for SED experiments. For all measurements involving nXRD, samples were deposited on X-Ray transparent, SiN windows from Norcada (product number NX7100C).

ots-$FAPbI_3$ film fabrication: Lead iodide (PbI_2, 0.346 g, 1.5 mmol), formamidinium iodide (FAI, 0.155 g, 1.8 mmol) and EDTA (5 mol% with respect to PbI_2) were dissolved in 0.5 mL of dimethyl sulfoxide (DMSO) under continuous stirring and heating at 75°C to obtain a clear dark yellow solution. The solution was then spin coated (4000 rpm for 40 seconds) on a UV-Ozone-cleaned glass substrate followed, in order to ensure film uniformity, by a gas quenching step in which nitrogen-gas was continuously blown on the surface of spinning films for 20 seconds, commencing 5 s after initial spinning (*42*). The approximate distance between the nitrogen-gun and film is ~7 cm for the first 10 seconds and then the distance between nitrogen-gun and film was reduced to ~5 cm and gas continued to be blown for a further 10 seconds. The spin coated films were annealed at 150°C for 1h in a nitrogen glovebox.

Control α-$FAPbI_3$ film fabrication: Lead iodide (PbI_2, 0.346 g, 1.5 mmol) and formamidinium iodide (FAI, 0.155 g, 1.8 mmol) was dissolved in 0.5 mL dimethyl sulfoxide (DMSO) under continuous stirring and heating at 75°C for 1h to obtain a transparent solution. The solution was then filtered through a PTFE syringe filter. The filtered solution was then spin coated (4000 rpm for 30 seconds) on a UV-Ozone-cleaned glass substrate followed by a the same gas quenching steps as for the ots-$FAPbI_3$ films. The spin coated films were annealed at 150°C for 1h in a nitrogen glovebox.

Synthesis of perovskites in powder form for NMR characterization: Lead iodide (PbI_2, 0.692 g, 1.5 mmol), formamidinium iodide (FAI, 0.310 g, 1.8 mmol) and EDTA (10 mol% with respect to PbI_2) were dissolved in 1 mL of dimethyl sulfoxide (DMSO) under continuous stirring and heating at 75°C for to obtain a clear dark yellow solution. The solution was then drop cast on a UV-Ozone-cleaned glass substrate. The drop-cast films were annealed at 150°C for 2-3 h until completely dry. The films were then scraped off to obtain dry ots-$FAPbI_3$ powder.

Control α-$FAPbI_3$ was prepared using mechanosynthesis (*43*, *44*) by grinding the reactants in an electric ball mill (Retsch MM−400) using an agate grinding jar (10 ml) and a ball (⌀10 mm) for 30 minutes at 25 Hz. The material was subsequently annealed at 170 °C for 5 minutes to remove grinding-induced defects and ensure that the material is fully in the α (black 3D perovskite) phase.

Scanning Electron Diffraction Measurements

Scanning electron diffraction (SED) data were acquired on the JEOL ARM300CF E02 instrument at ePSIC, Diamond Light Source with a Merlin/Medipix pixelated STEM detector for fast scanning electron diffraction. Utilizing this detector and the following experimental parameters: accelerating voltage = 200 kV; nanobeam alignment (~1 mrad convergence angle); electron probe ~5 nm; probe current ~3.1 pA; scan dwell time 1 ms; camera length 15 cm, we can achieve an electron dose per scan of ~10 $eÅ^{-2}$ at 150 kX magnification when approximating the beam shape as a circle with a diameter of ~5 nm. This accumulated dose is almost an order of magnitude lower than the lowest reported threshold at which the crystal structure of $FAPbI_3$ begins to change (66 $eÅ^{-2}$) (*45*). See Supplementary Note 1 for further discussion on possible origins of superstructure reflections beyond octahedral tilting, including beam induced artefacts.

SED data were calibrated and corrected for elliptical distortions using reference data acquired on an Au cross grating. In SED, under our experimental conditions, 1 pixel on the Merlin/Medipix pixelated STEM detector is ~0.0059 $Å^{-1}$. SED diffraction data was analyzed in pyXem (*46*). In the manuscript, we refer to annular dark field (ADF) images in reference to SED data presented in Fig. 2. ADFs are reconstructed from SED data by plotting the integrated diffracted intensity as a function of probe position, excluding the directly transmitted beam. All diffraction patterns presented in the main text are processed by taking the square root of the image intensity to make it easier to resolve weak reflections. The temperature in the electron column during data acquisition was ~ 19° C. For ots-$FAPbI_3$, data was acquired on multiple areas of 3 different samples across 1 experimental run and similar distributions of tilted and untilted/hexagonal structures were observed in each. For $(Cs_{0.05}FA_{0.78}MA_{0.17})PbI_3$ samples, data was acquired on multiple areas of 3 different samples at 2 experimental runs and the same octahedral tilt patterns were observed across all examined patterns. For $(Cs_{0.05}FA_{0.78}MA_{0.17})Pb(I_{0.83}Br_{0.17})_3$ samples, data was acquired on multiple areas of 9 samples across 4 experimental runs and the same octahedral tilt patterns were observed across all examined patterns. For $FA_{0.7}Cs_{0.3}Pb(I_{0.9}Br_{0.1})_3$ samples, data was acquired on multiple areas of 3 different samples at 2 experimental runs and the same octahedral tilt patterns were observed across examined patterns.

Nano X-ray Diffraction Measurements

Measurements were performed on the i14 Hard X-ray Nanoprobe beamline at Diamond Light Source Ltd., Didcot, UK using a 19 keV monochromated X-ray beam (*47*).The diffracted X-rays were collected in a transmission geometry with an Excalibur 3M detector consisting of 3 Medipix 2048 x 512 pixel arrays. The step size for the measurements was 50 nm and the dwell time was 0.75 s per point. All samples were stored in a nitrogen filled glovebox before measurement, and held under a nitrogen flow during measurements. 2D diffraction patterns were calibrated with a CeO_2 reference standard and radially integrated in the Data Analysis Workbench (DAWN) (*45*). Spatially resolved 1D nXRD patterns were then further analyzed in the open source Python packages Hyperspy and pyXem (*46*, *48*). In the manuscript and supporting materials, we refer to virtual dark field (VDF) images. Virtual dark field images are generated by plotting the diffracted intensity of a selected Bragg peak as a function of probe position, revealing the regions of a scan where diffracted intensity from that specific peak is highest. Using the VDF as a mask extracting diffraction patterns from just the regions of the scan where diffracted intensity occurs in the peak of interest can substantially improve signal-to-noise. All nXRD measurements were performed at room temperature (~ 20 ° C). 3 nXRD samples across 2 experimental runs were examined.

First-Principles Simulations of Phase Intermixing

All octahedral layers in the cubic and tetragonal phases share their corners, and all octahedral layers in the hexagonal phase share their faces with neighboring layers. At an interface between them, the formation of a single octahedral layer that shares its corner on one side and its face on the other side is inevitable. The thermodynamic cost for forming this interfacial layer (E_{intf}) represents a lower bound to phase transition barrier from corner sharing phase to face sharing phase. We calculated this value following,

$$E_{\mathrm{intf}} = \frac{1}{2}[(2n+2)E_{\mathrm{mixed}} - nE_{\mathrm{corner}} - nE_{\mathrm{face}}]$$

where E_{mixed}, E_{corner}, and E_{face} are the density functional theory (DFT) total energies for mixed, corner sharing, and face sharing phases per formula unit, respectively, n is the number of octahedral layers for corner sharing and face sharing in the mixed phase supercell. In our calculation, we used a supercell that contains 12 octahedral layers, and therefore n was set to 5. Following this procedure, we obtained a barrier height of 26 meV/f.u. for the cubic to hexagonal phase transition and of 75 meV/f.u. for the tetragonal to hexagonal phase transition (Fig. 2B). The calculations therefore confirm that the cubic-to-hexagonal transition is more energetically accessible than the tetragonal-to-hexagonal transition, which originates from both a larger thermodynamic driving force for the cubic to hexagonal transition and a lower phase transition barrier height.

The underlying DFT calculations were performed using the Vienna Ab initio Simulation Package (VASP) (*49*, *50*) where projector augmented-wave (PAW) (*51*, *52*) pseudopotentials were employed to treat core atomic states, and the valence electron configurations of Cs, Pb, and I are explicitly considered as $5s^25p^66s^1$, $5d^{10}6s^26p^5$, and $5s^25p^5$, respectively. The

convergence criteria of the total energy was set to within 10^{-6} eV and the forces on each of the atoms was set to 10^{-2} eV/Å.

For all geometry optimizations, the Perdew–Burke–Ernzerhof exchange-correlation functional revised for solids (PBEsol) (*53*) was used where a plane-wave kinetic cutoff energy of 300 eV was set. To model the cubic/hexagonal systems, we constructed superlattice models that contains 60 atoms (i.e. 12 formula units), while superlattice models with 240 atoms (i.e. 48 formula units) were constructed to model the mixed cubic/hexagonal systems. $CsPbI_3$ was chosen as a model composition to avoid issues with molecular reorientations and disorder. The Brillouin-zone integrations were performed with a Γ-centered k-point grid of 6 × 6 × 2 for the cubic/hexagonal systems and of 3 × 3 × 2 for the tetragonal/hexagonal systems. To prevent undesirable distortion of corner-sharing phases to lower (below tetragonal) symmetry structures, we fixed the tilting patterns of the corner-sharing layers in our superlattice models and allowed only the face-sharing layers to be relaxed during structural optimizations where the lattice vectors of superlattice unit cells were constrained to the hexagonal cell shape ($a_0 = b_0 \neq c_0, \alpha = \beta = 90°, \gamma = 120°$). Optimized superlattice structures have been made accessible in an on-line repository at https://doi.org/10.5281/zenodo.5511782.

Nuclear Magnetic Resonance (NMR) and Nuclear Quadrupole Resonance (NQR) Measurements

Room temperature liquid-state ^{1}H (500.2 MHz) and ^{207}Pb (104.6 MHz) spectra were recorded on a Bruker Avance III HD 11.7 T spectrometer equipped with a BBO Smart Probe. ^{1}H shifts were referenced using the residual CH_3 signal of toluene-d_6 (2.51 ppm) as a secondary reference. ^{207}Pb spectra were referenced to aqueous $Pb(NO_3)_2$ at -2963 ppm. A recycle delay of 0.1 s was used to record the liquid-state ^{207}Pb spectra and between 1900 and 4096 scans were acquired. The spectra in the main text (Fig. 3E) were plotted with 1000 Hz of Lorentzian apodization.

Room temperature solid-state ^{13}C (125.8 MHz), ^{207}Pb (83.8 MHz) spectra were recorded on a Bruker Avance Neo 9.4 T spectrometer equipped with a 4.0 mm CPMAS probe. ^{13}C chemical shifts were referenced using solid adamantane as a secondary reference (δ_{CH2} = 38.48 ppm) (*54*). The ^{207}Pb and ^{14}N spectra were detected using an echo sequence and referenced based on the ratios of gyromagnetic ratios using the unified chemical shift scale of IUPAC. Calibrated RF strengths were as follows: ^{14}N (50 kHz), ^{207}Pb (100 kHz). 51 kHz of ^{1}H decoupling was applied during acquisition in the ^{1}H-^{13}C CP experiments and a contact time of 1 ms was used. All solid-state experiments were carried out at 12 kHz MAS unless stated otherwise. Further experimental details are given in Table S1. ^{127}I NQR measurements were carried out using an Avance III HD console and a 4 mm CPMAS probe on non-spinning samples. A Hahn echo sequence, 167 kHz RF strength, an echo time of 5 μs, and a recycle delay of 0.01 s were used. In cases where the signal width exceeded the RF strength, variable offset cumulative spectra (VOCS) acquisition was used. Further experimental details are given in Table S1.

Infrared Nanospectroscopy (AFM-IR) mapping measurements

Infrared nanospectroscopy measurements were performed by a customized nanoIR2 (Anasys Instrument, USA) systems capable of working in ORS-nanoIR mode (*55*). The sample

morphology was scanned by the AFM-IR microscopy system, with a rate line within 0.05-0.5 Hz and in contact mode. A silicon gold coated PR-EX-nIR2 (Anasys, USA) cantilever with a nominal radius of 30 nm and an elastic constant of about 0.2 N/m was used. To use gold-gold rod-like antenna the IR light was polarized perpendicular to the surface of deposition.

All maps were acquired with a resolution between 10-30 nm/pixel. Maps were acquired by using phase loop (PLL) tracking of the contact resonance between the sample and the cantilever; in order to measure purely the chemical signal avoiding cross-talks with mechanical properties of the sample (*55*, *56*). The AFM images were treated and analyzed using SPIP software. The height images were first order flattened, while IR and stiffness related maps where only flattened by a zero-order algorithm (offset). All measurements were performed at room temperature and with laser power between 0.5-5% of the maximal one and under controlled Nitrogen atmosphere with residual real humidity < 5%.

X-Ray Diffraction (XRD): Bulk X-ray diffraction measurements were performed on a Bruker X-Ray D8 Advance diffractometer employing Cu Kα radiation (λ = 1.54 Å) was used.

UV-Vis absorption: UV-Vis absorption measurements of ots-$FAPbI_3$ thin films were performed on a Shimadzu UV-3600 Plus double-beam spectrophotometer utilizing an integrating sphere to account for scattering effects.

Photoluminescence: Photoluminescence emission spectra of the thin films were recorded on an Edinburgh Instruments FLS1000 PL spectrometer with either 500-nm excitation wavelength using a Xe lamp or with a continuous-wave diode laser at 520 nm using an Andor iDus Si detector.

Time-correlated single photon counting (TCSPC): TCSPC results were obtained using an Edinburgh Instruments Life Spec system, FLS1000. A picosecond pulsed diode laser (EPL-510, Edinburgh Instruments), with a wavelength of 505.8 nm and pulse width of 75 ps, was used for excitation. A repetition rate between 500 kHz to 50 kHz was used.

An iCCD, a gated intensified CCD camera (Andor iStar DH740 CCI-010) connected to a calibrated

grating spectrometer (Andor SR303i) was used to record time-resolved PL spectra. The excitation wavelength was 400 nm with narrow bandwidth, generated by frequency-doubling 800-nm emission from a Ti: sapphire optical amplifier (1 kHz repetition rate, 90 fs pulse width). The incident pulse energy was 0.45 μJ/cm^2/pulse. The effective beam diameter of the excitation spot was 647 μm.

External stress measurements:

Ambient air: Thin films of ots-$FAPbI_3$ perovskites were fabricated on glass (thin coverslip) substrates to perform ambient air stability measurements. All bulk XRD measurements of the thin films were performed in ambient air and films were stored in a loosely capped plastic case on laboratory desk where ambient conditions were maintained. 3 samples across 2 experimental runs from 3 batches were examined for ambient air stability.

Thermal stability: To investigate the thermal stability of ots-$FAPbI_3$, we fabricated thin films on glass substrates and the fabricated samples were heated at 100 ^oC on a hot plate in ambient air for 24h. We covered the samples with a glass petri dish (upside down) to avoid unintentional exposure to residual organic solvents. We performed XRD and TCSPC measurements in ambient air before and after thermal stress. 6 samples across 3 experimental runs from 2 batches were exposed to 100 ^oC in ambient air to check thermal stability of ots-$FAPbI_3$.

Light stability: In order study the light stability, we fabricated ots-$FAPbI_3$ perovskite thin films on ITO-substrates. We used a glass petri dish (upside down) to cover samples to avoid exposure to residual solvents. The samples were exposed to 1-sun illumination (AM1.5) using a solar simulator for 100h in ambient air. We performed TCSPC and XRD measurement in ambient air before and after the illumination. 4 samples across 2 experimental runs from 2 batches were used to study the light stability.

Supplementary Text

Supplementary Note 1: Octahedral tilting and crystal phase assignment.

In the manuscript, we assign the structure of $(Cs_{0.05}FA_{0.78}MA_{0.17})Pb(I_{0.83}Br_{0.17})_3$ and $(Cs_{0.05}FA_{0.78}MA_{0.17})PbI_3$ to be tetragonal *P4/mbm*. Though we cannot discount the possibility that some local regions in a given triple cation perovskite thin film exhibit other static tilt systems or dynamic symmetry breaking (*57*), the vast majority of electron diffraction patterns that we observe in our study (hundreds across many different samples) as well as X-ray diffraction data are consistent with assignment to a tetragonal *P4/mbm* structure. Relative to the *Pm-3m* cubic structure with a lattice parameter of 6.3 Å, the *P4/mbm* structure can be understood as a $\sqrt{2}$ x $\sqrt{2}$ x 1 superstructure transformation resulting in new lattice parameters of ~ 8.91 Å x 8.91 Å x 6.3 Å. Superstructure reflections can also arise from double diffraction (dynamical scattering), electron-beam induced damage or cation ordering.

Double Diffraction

In the zone axis patterns, we present in Fig. 1 and Fig. S1, S3 and S8, there are no double diffraction routes that would lead to the appearance of the observed superstructure reflections: The indices of double diffraction spots are given by the sum of the indices of two component primary Bragg spots such that diffraction spots of the form h_1+h_2, k_1+k_2, l_1+l_2 are possible double diffraction spots, where $h_1k_1l_1$, $h_2k_2l_2$ are any two allowed primary Bragg spots (*58*).

Beam Induced Changes

Electron beam induced damage can manifest as experimentally observed superstructure reflections in perovskite compositions such as $MAPbI_3$ due to the creation of ordered defects (*22*). However, the reported doses at which superstructure reflections begin to appear in $MAPbI_3$ perovskites are over an order of magnitude greater than those employed in this study. Additionally, these beam damage induced superstructure reflections are not consistent with the superstructure reflections that indicate the presence of octahedral tilting (*20*, *22*). In reports of beam damage in $FAPbI_3$ like perovskites, which are more similar to the perovskites studied in this paper than $MAPbI_3$, a loss of crystallinity is observed as the primary effect of electron beam induced damage, rather than the formation of any superstructure reflections. This loss of crystallinity begins to occur at electron doses ~ an order of magnitude greater than those employed here (*45*). Finally, alloyed perovskite compositions with high Cs^+ fractions have been reported to possess a tilted tetragonal structure at room temperature (*21*). Examining an evaporated $FA_{0.7}Cs_{0.3}Pb(I_{0.9}Br_{0.1})_3$ perovskite (Fig. S3), which according to previous work should possess a tetragonal structure (*21*), reveals the presence of superstructure reflection similar to those observed in the triple cation and $FAPbI_3$ samples in this manuscript. We note that the degree of tilting in the $FA_{0.7}Cs_{0.3}Pb(I_{0.9}Br_{0.1})_3$ is much larger than that in the triple cation and $FAPbI_3$ samples, as revealed by the brighter superstructure intensity relative to the primary Bragg peaks (Fig. S3) in the $FA_{0.7}Cs_{0.3}Pb(I_{0.9}Br_{0.1})_3$ perovskite when compared against the triple-cation and $FAPbI_3$ (Fig. 1) perovskites. This brighter intensity in the superstructure reflections (larger degree of tilting) is what has allowed octahedral tilting in $FA_{0.7}Cs_{0.3}Pb(I_{0.9}Br_{0.1})_3$ to be previously observed macroscopically (*21*). Collectively, these observations and results strongly suggest that the superstructure reflections we observe in the

triple cation and $FAPbI_3$ perovskites are intrinsic to the room temperature structure and indicative of octahedral tilting.

Cation Ordering

In general, cation ordering in perovskites is more common on the B site than the A site (*59*). As all structures interrogated in this manuscript are of the form ABX_3, $AA'BX_3$ or $AA'A''BX_3$, we can rule out any ordering on the B site. Additionally, we can rule out A-site cation ordering as the source of superstructure reflections in the single A-site cation $FAPbI_3$. As the symmetry of the superstructure reflections observed between $FAPbI_3$ and triple cation compositions are mostly similar, this indicates that the source of superstructure reflections in the triple cation perovskites is likely also octahedral tilting. While A-site cation ordering can occasionally be driven by octahedral tilting, this typically only occurs in $a^+a^+a^+$, $a^+a^+c^-$, $a^0b^+b^+$, and $a^0b^+b^-$ (glazer notation) tilt systems. In this manuscript we mostly observe $a^0a^0c^+$ (*P4/mbm*) tilt systems making it unlikely that octahedral tilting in the triple cation perovskite is driving cation ordering. In addition, when A-site cation ordering does occur, it typically results in superstructure reflections appearing in the $<110>_c$ zone axis patterns, which we do not observe (Fig. S4, S5, S6) (*20*, *60*). While we cannot rule out that some local regions of a given perovskite film that we have examined deviate from these observations, we can conclude that the superstructure reflections we observe cannot be attributed to cation ordering alone, and that it is unlikely that cation ordering and octahedral tilting are occurring in conjunction.

Origin of Octahedral Tilting: Cation vs Anion Mixing

Anions such as halides certainly affect lattice symmetry. However, in the specific case of formamidinium lead halides, $FAPbI_3$ and $FAPbBr_3$ have both been identified as possessing a cubic *Pm-3m* structure from Neutron diffraction studies (*25*, *61*). Additionally, it is proposed that iodide and bromide mixing in formamidinium lead halides leads to solid solution which are cubic for any I:Br ratio and follow Vegard's law (*62*). For the triple cation materials studied here, $Cs_{0.05}FA_{0.78}MA_{0.17}Pb(I_{0.83}Br_{0.17})_3$, can be formally considered as cubic formamidinium lead iodide-bromide doped with Cs^+ and MA^+, while $Cs_{0.05}FA_{0.78}MA_{0.17}PbI_3$ possesses only a single halide and the material can be formally considered as cubic $FAPbI_3$ doped with Cs^+ and MA^+. Both materials exhibit the same octahedral tilting patterns, regardless of anion composition. Collectively, these observations suggest that, in the case of the FA-rich materials interrogated here, octahedral tilting is driven primarily by mixing of the A-site cation rather than the anion. This is not, however, to say that the anion cannot additionally influence the degree of observed octahedral tilting. In Fig. S8, we extract two grains oriented close to the $[100]_c$ zone axis in both $Cs_{0.05}FA_{0.78}MA_{0.17}Pb(I_{0.83}Br_{0.17})_3$ and $Cs_{0.05}FA_{0.78}MA_{0.17}PbI_3$. We then compare the same sets of superstructure reflections in each composition to show that the intensity of superstructure reflections relative to primary Bragg peaks is generally stronger in the single halide $Cs_{0.05}FA_{0.78}MA_{0.17}PbI_3$ compared to the mixed-halide $Cs_{0.05}FA_{0.78}MA_{0.17}Pb(I_{0.83}Br_{0.17})_3$. This suggests that octahedral tilting is stronger in the single-halide than the mixed-halide sample. However, we note that for the same reasons as those identified in Supplementary Note 2 in regards to quantitatively determining the degree of octahedral tilting (i.e. dynamical scattering and lack of precession preventing quantitative peak intensity extraction) this is a qualitative and not a quantitative observation. Elucidation of the

full effect of anion mixing on the degree of octahedral tilting would require either Neutron diffraction studies of single crystal samples or precession electron diffraction studies of thin films.

Diffraction Pattern Indexation:

To index an electron diffraction pattern two or more experimental vectors and the angles between the vectors are sufficient to produce an accurate indexation of a known structure (*58*). Where multiple structures exist as possible solutions, the process is more complicated. Our method is as follows: For a given electron diffraction pattern, following calibration, the lengths of experimental vectors were compared against a list (generated in CrystalMaker software) of the predicted vector lengths of every structure of interest (thousands of vectors per structure). Any predicted vector length that did not match the experimentally observed vector lengths (+/- 10 %) were immediately discarded as not being a possible match (In the case where after this initial step, a possible structure did not possess any vector lengths that matched those experimentally observed, it was immediately discounted as being a possible structure match). In scenarios where forbidden reflections could, in principle, arise from dynamical scattering effects such as double diffraction, the brightest reflections in the experimental diffraction patterns were chosen for indexation as these are highly likely to be primary Bragg peaks. Though we note that, none of the diffraction patterns presented in this text possess diffraction spots arising from double diffraction that would affect our indexations). Then, for a pair of given remaining predicted vectors in a given possible structure, both the cross product (which corresponds to the electron beam direction and thus the zone axis direction which would allow the diffraction spots corresponding to our predicted pair of vectors to appear in a diffraction pattern) and the inter-vector angles are calculated (*63*). The calculated inter-vector angle is compared to our experimentally observed inter-vector angle. If it deviates by greater than 1° from our experimentally observed angle, then the zone axis associated with this particular vector pair is discarded and we move on to the next potential vector pair. Typically, after this filtration process, a single, or handful of possible zone axis indexations across all possible structures remain. We then simulate these remaining possible zone axis patterns in the open source python package diffsims (*64*) and the software package SingleCrystal and closely compare the simulations to our experimentally observed diffraction pattern in order to determine the correct indexation. Structures considered for hexagonal assignment were the 2H, 4H, and 6H perovskite structures as these have all been experimentally observed in FA-rich perovskites and are associated steps on the crystallization (*2*) and degradation pathway (*3*) of 2H to Pm-3m and Pm-3m to 2H, respectively.

Supplementary Note 2: Determination of degree of octahedral tilting from nXRD.

The degree of octahedral tilting in a given sample will directly affect the intensity of observed superstructure reflections in diffraction measurements. Due to the dynamical nature of electron diffraction and the fact that we do not utilize precession in the acquisition of our scanning electron diffraction data, we cannot extract reliable quantitative intensities from our electron diffraction patterns. Quantitative intensities can readily be extracted from XRD patterns, provided that orientations and Bragg peaks are uniformly sampled. In spatially resolved nXRD where the polycrystalline film is likely textured within our scan region, and where we cannot

rock the sample through the incident x-ray beam to obtain fully integrated Bragg diffraction peaks, quantitatively analyzing diffraction peak intensities becomes challenging, and is further complicated by the very weak nature of the superstructure reflections of interest. To provide some estimate of octahedral rotation, we formed virtual dark field (VDF) images of the $(121)_r$ peak across a nXRD scan to determine regions of the sample where grains were in an orientation such that the Bragg condition for $(121)_t$ was satisfied and diffracted intensity was intense enough that it could be observed (Fig. S7). We then thresholded this VDF image and used it as a mask to extract 26 pixels from our nXRD scan (Fig. S7), all displayed of which displayed $(121)_t$ diffracted intensity. We did the same for the $(100)_c$ peak and obtained hundreds of pixels that exhibited $(100)_c$ diffracted intensity, but chose the 26 brightest pixels, which we hypothesize are the closest approximation of the fully integrated intensity of $(100)_c$ (Fig. S7). We averaged these 26 pixels to obtain the plot used for comparison in Fig 1G and did the same for the 26 $(121)_t$ pixels, which is plotted in Fig. 1F. Using this methodology, we observed that $I_{(121)t}$ was 0.75% that of $I_{(100)c}$, which corresponds to an octahedral rotation of ~0.75 degrees about the c-axis of the unit cell as derived from simulations for a variety of different octahedral rotations about the c-axis of the unit cell (*P4/mbm* spacegroup) in the software package Crystal Diffract. To place an approximate upper bound on the degree of octahedral tilt in the sample, we compared the average peak intensity extracted from the 26 pixels of $(121)_t$ to the average peak intensity of every pixel (598) where intensity from the $(100)_c$ peak is observed. Here we observed that $I_{(121)t}$ was 3.5% that of $I_{(100)c}$, which corresponds to an octahedral rotation of ~ 2.75 degrees about the c-axis of the unit cell. More precise estimations than this would require either Neutron diffraction experiments with single crystal samples or precession electron diffraction of thin film samples.

Supplementary Note 3: Discussion of the Pb^{2+}-EDTA interaction based on ^1H liquid-state NMR.

In a solution of EDTA in DMSO-d_6, owing to the unimpeded rotation of the neighboring bonds, the acetate methylene protons (-N-C**H$_2$**-COOH) are magnetically equivalent and appear as a singlet in the ^1H NMR spectrum. On the other hand, in metal chelates the rotation of the -CH_2- group becomes restricted and the two protons become magnetically inequivalent since their local environments are slightly different. This leads to the appearance of a so-called AB spin pattern, in which the frequency separation between the peaks is comparable to the J-coupling strength between the two protons. Depending on the ratio of these two parameters, the AB patterns resembles a quartet or a doublet. AB patterns of the acetate methylene protons of EDTA have been previously observed in EDTA chelates with Pb^{2+} and other metals (*37*). Since we do not observe an AB spin pattern, we conclude that a long-lived hexadentate Pb^{2+}-EDTA chelate does not form. Instead, we attribute the relative shift of the methylene signals of EDTA to changes in the equilibrium protonation of the EDTA molecule. Indeed, in aqueous solutions, the position of the EDTA methylene signals depends on pH, in keeping with the presence of multiple stages of protonation (cf. the reference above). A complex is still likely formed, but if the EDTA is partially protonated, may not involve all six binding sites of the $EDTA^{4-}$ ligand. We collectively refer to these interactions as Pb^{2+}-EDTA interaction.

Supplementary Note 4: Sensitivity of ^{14}N MAS NMR structural changes.

The line shape of ^{14}N MAS NMR spectra of MA and FA in 3D halide perovskites is sensitive to incorporation of dopants into the perovskite structure (*35*). For example, substantial changes have been demonstrated for $MAPbI_3$ doped with 5 mol% guanidinium and $FAPbI_3$ doped with 10 mol% Cs^+. On the other hand, virtually no changes have been observed between α-$FAPbI_3$ and FA-based Ruddlesden-Popper phases with an adamantyl-based spacer cation.

These results suggests that, while ^{14}N is a highly sensitive probe of dopant incorporation into the perovskite structure via changes in the A-site cation cage symmetry, it may not always be able to detect some of the more subtle changes induced by templating ligands. In the present case, there is no difference between the ^{14}N MAS NMR spectra of the control α-$FAPbI_3$ and ots-$FAPbI_3$. We therefore conclude that (1) EDTA does not incorporate into the 3D perovskite structure since this would lead to substantial line shape changes, as is the case for Cs-doped $FAPbI_3$, and (2) the tetragonal distortion identified by SED and nXRD is too small to be resolvable by ^{14}N MAS NMR.

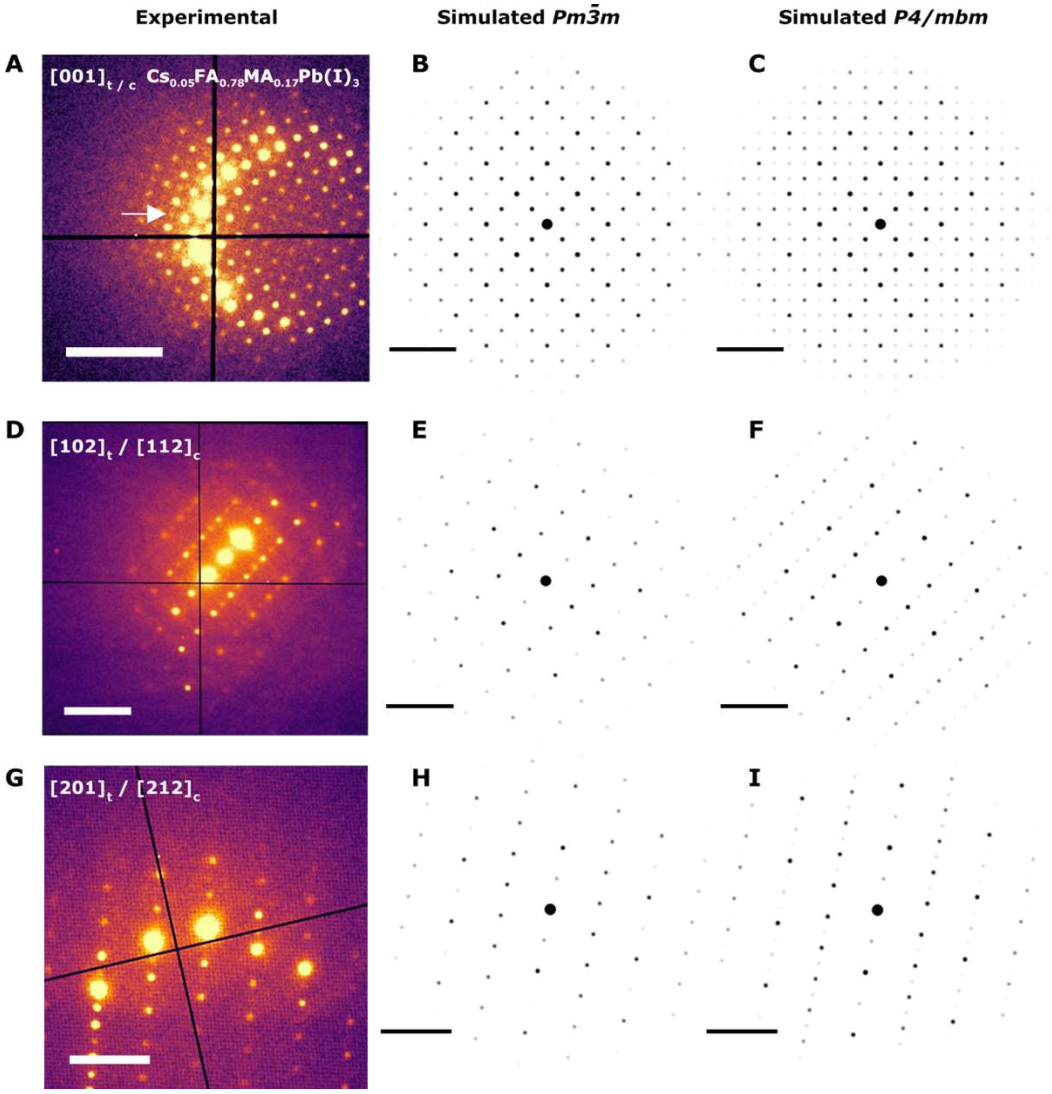

Fig. S1. (A) Experimental ED pattern of a $(Cs_{0.05}FA_{0.78}MA_{0.17})PbI_3$ thin film perovskite oriented near the $[001]_{t/c}$ zone axis. The same superstructure reflections are observed in this composition as in the $(Cs_{0.05}FA_{0.78}MA_{0.17})Pb(I_{0.83}Br_{0.17})_3$ shown in the main text **(B)** Simulated $[001]_c$ electron diffraction pattern. No superstructure reflections visible **(C)** Simulated $[001]_t$ electron diffraction pattern. Superstructure reflections are visible and match those experimentally observed in (A) and Fig. 1A. **(D)** Experimental ED pattern of a $Cs_{0.05}FA_{0.78}MA_{0.17})Pb(I_{0.83}Br_{0.17})_3$ perovskite oriented near the $[102]_t$ /$[112]_c$ zone axis. Superstructure reflections are visible. **(E)** Simulated $[112]_c$ electron diffraction pattern. No superstructure reflections are visible. **(F)** Simulated $[102]_t$ electron diffraction pattern. Superstructure reflections are visible and match those experimentally observed in (D). **(G)** Experimental ED pattern of a $(Cs_{0.05}FA_{0.78}MA_{0.17})PbI_3$ thin film perovskite oriented near the $[201]_t$/$[212]_c$ zone axis. Superstructure reflections are visible. **(H)** Simulated $[212]_c$ electron diffraction pattern. No superstructure reflections are visible. **(I)** Simulated $[201]_t$ electron diffraction pattern. Superstructure reflections are visible and match those experimentally observed in (G). Scalebar in A = $0.8Å^{-1}$. Scalebars in all other panels = $0.5Å^{-1}$

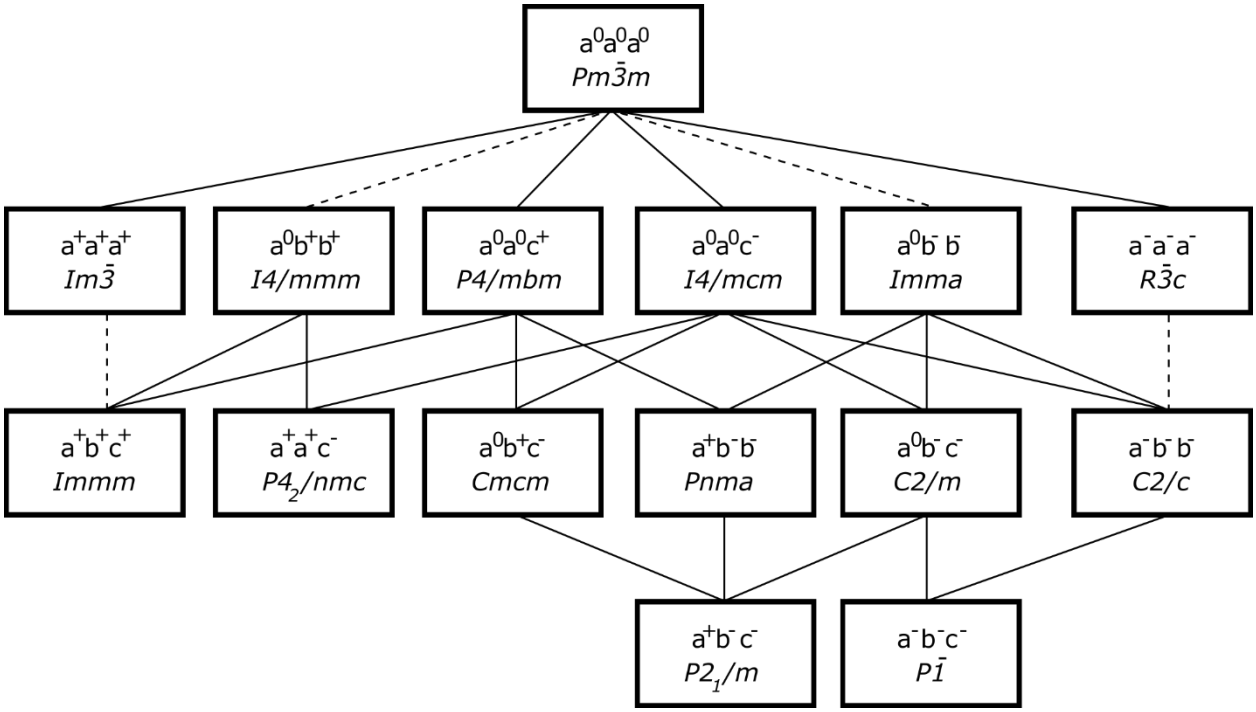

Fig. S2. Distinct tilt systems, and group-subgroup relationships between them, in ABX_3 perovskites. Reproduced from (*20*)

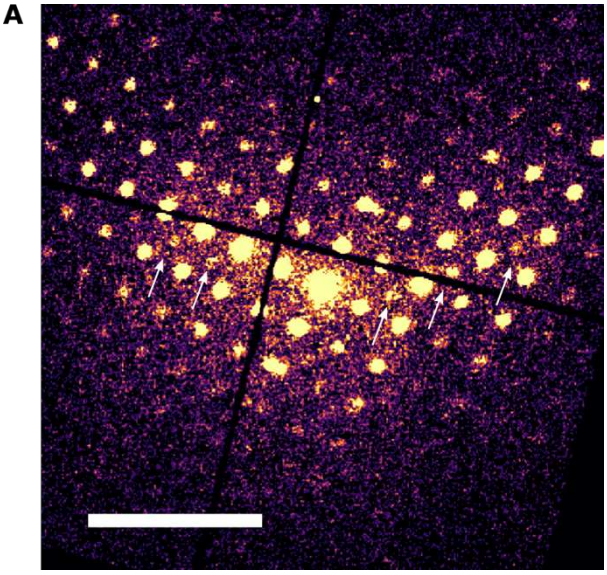

Fig. S3. Superstructure reflections in $FA_{0.7}Cs_{0.3}Pb(I_{0.9}Br_{0.1})_3$ thin films deposited by vapor deposition indicating the presence of octahedral tilting. (A) Diffraction pattern extracted from a grain oriented near the $[001]_c$ zone axis. Reflections forbidden from appearing in a cubic space group are indicated by white arrows. The symmetry of these superstructure reflections are the same as those observed in solution processed triple cation films shown in Fig. 1A and Fig. S1.

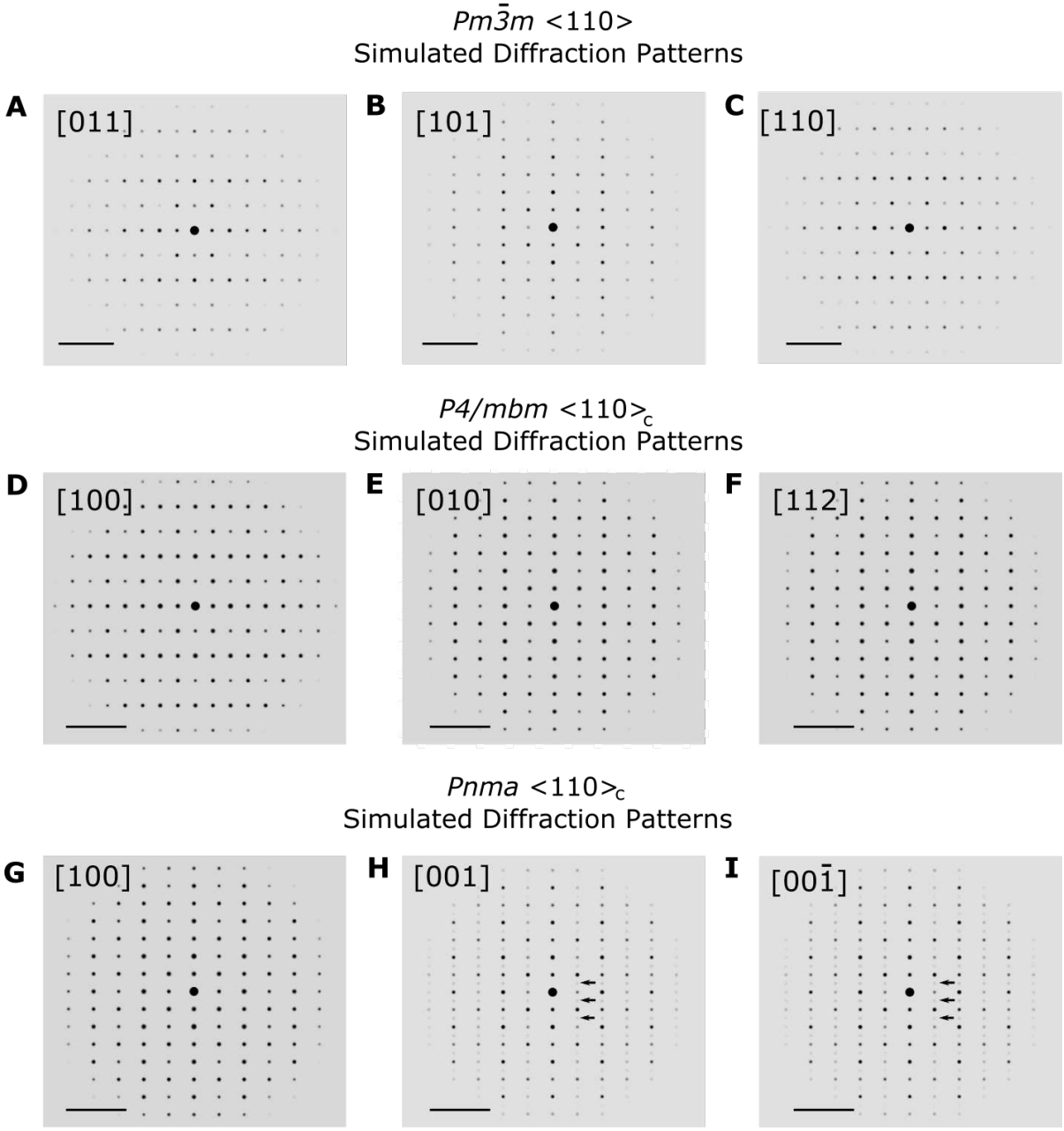

Fig. S4. Selection of simulated <110>$_c$ diffraction patterns from *Pm-3m, Pnma* and *P4/mbm* space groups. Simulated **(A)** $[011]_c$ zone axis of *Pm-3m* **(B)** $[101]_c$ zone axis of *Pm-3m* **(C)** No superstructure reflections are visible in <110>$_c$ zone axis patterns of cubic *Pm-3m* spacegroup. Simulated **(D)** $[100]_t$ zone axis of *P4/mbm*, **(E)** $[010]_t$ zone axis of *P4/mbm* and **(F)** $[112]_t$ zone axis of *P4/mbm*. No superstructure reflections are observed in <110>$_c$ zone axis patterns of *P4/mbm* tetragonal space group. Simulated **(G)** $[100]_o$ zone axis of *Pnma*, **(H)** $[001]_o$ zone axis of *Pnma* (superstructure reflections are visible, a subset are indicated by arrows), **(I)** $[00\text{-}1]_o$ zone axis of *Pnma* (superstructure reflections are visible, a subset are indicated by arrows). Scalebars are 0.5 Å^{-1}.

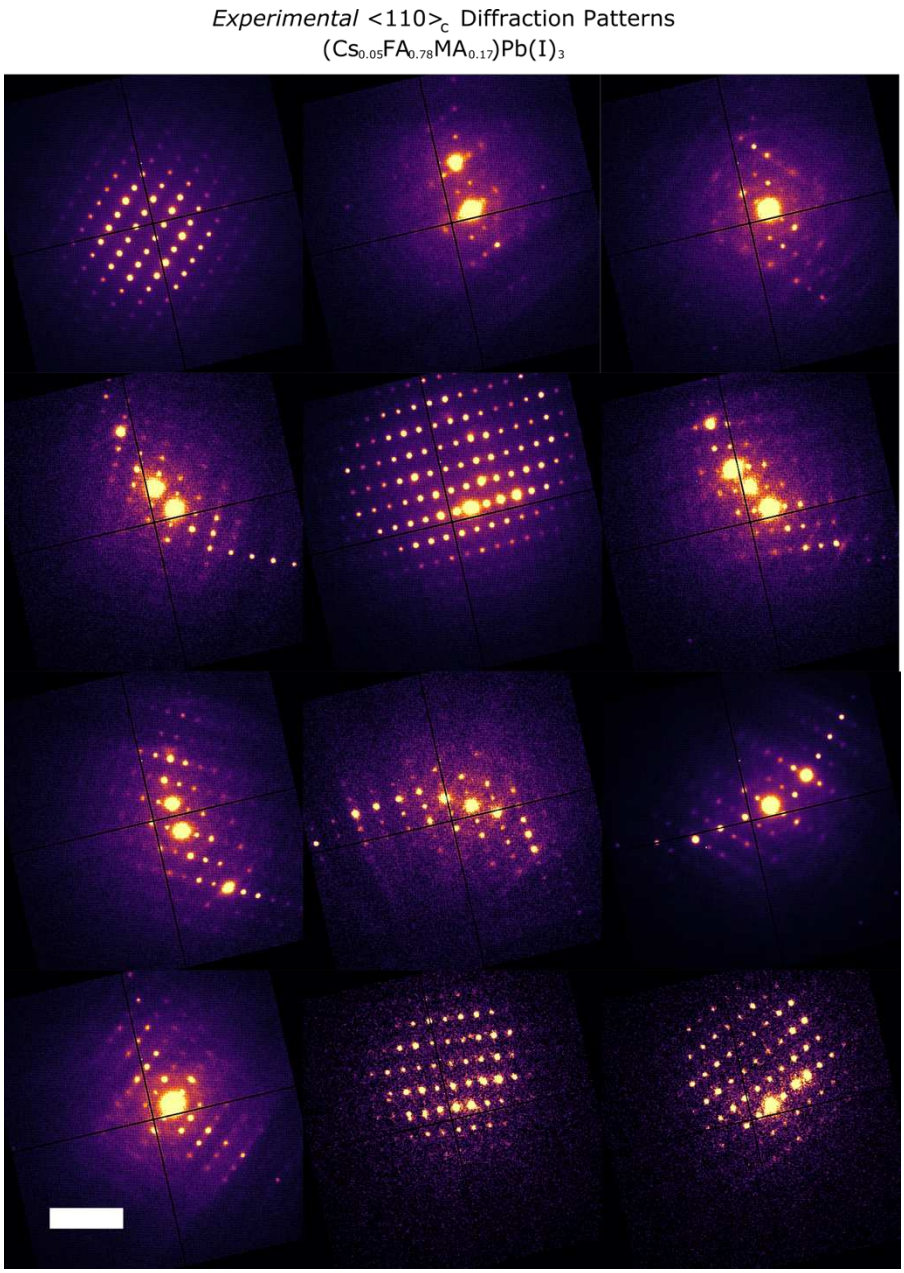

Fig. S6. Selection of <110>$_c$ zone axis experimentally measured ED patterns for $(Cs_{0.05}FA_{0.78}MA_{0.17})PbI_3$ thin films, none of which show superstructure reflections. Scalebar is 0.7 Å^{-1}.

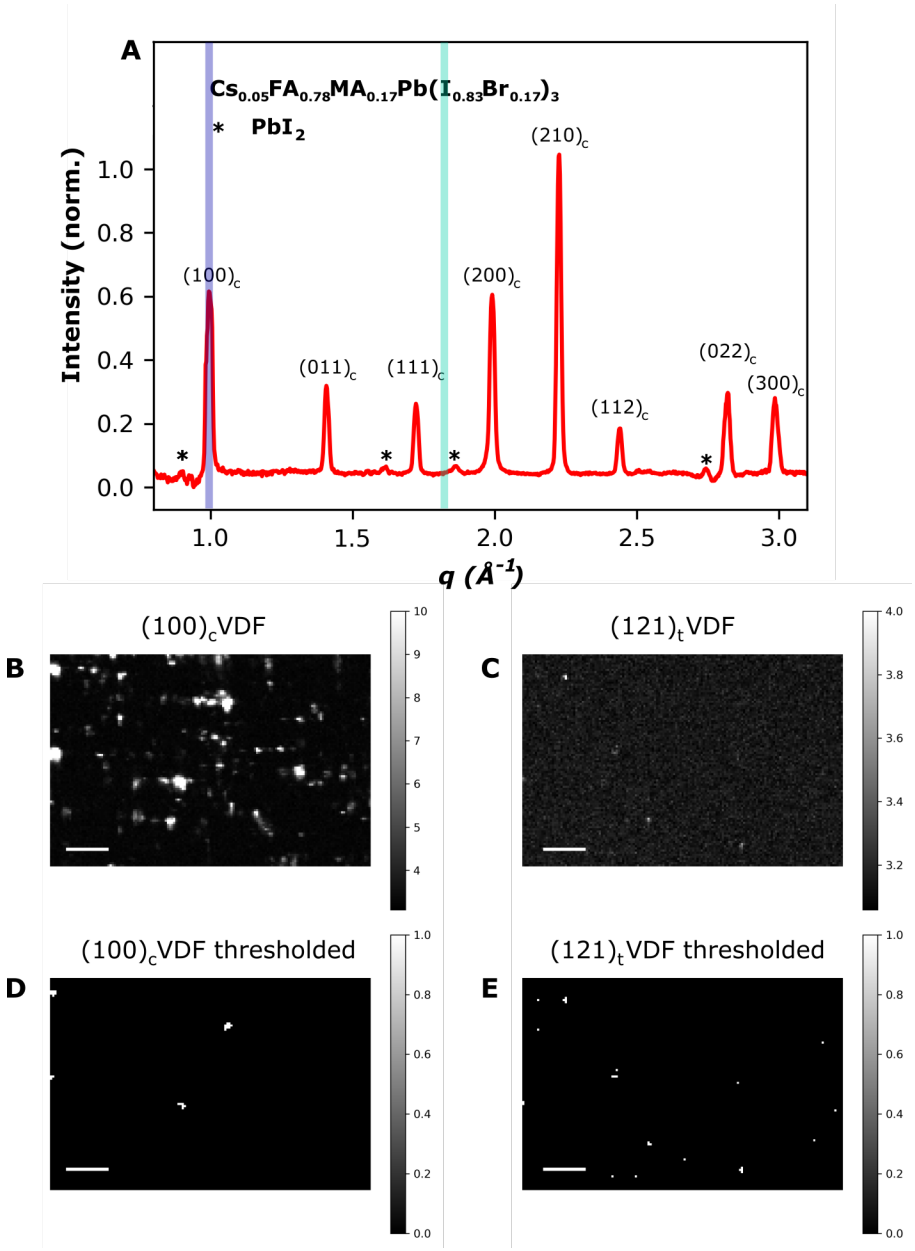

Fig. S7. Nano X-ray Diffraction (nXRD) virtual dark field (VDF) imaging of $(Cs_{0.05}FA_{0.78}MA_{0.17})Pb(I_{0.83}Br_{0.17})_3$ thin films. (A) Average diffraction pattern extracted from the 15 x 10 µm region shown in (B), (C), (D), and (E). The same average nXRD pattern is shown in Fig. 1E. **(B)** VDF image showing the diffracted intensity of the $(100)_c$ plane across the scanned region. To form the VDF, diffracted intensity is extracted from the purple window shown in (A) at every probe position in the scan. **(C)** VDF image showing the diffracted intensity of the $(121)_t$ plane across the scanned region. To form the VDF, diffracted intensity is extracted from the green window shown in (A) at every probe position in the scan. Scalebars in (B), (C), (D), and (E) are 2 µm.

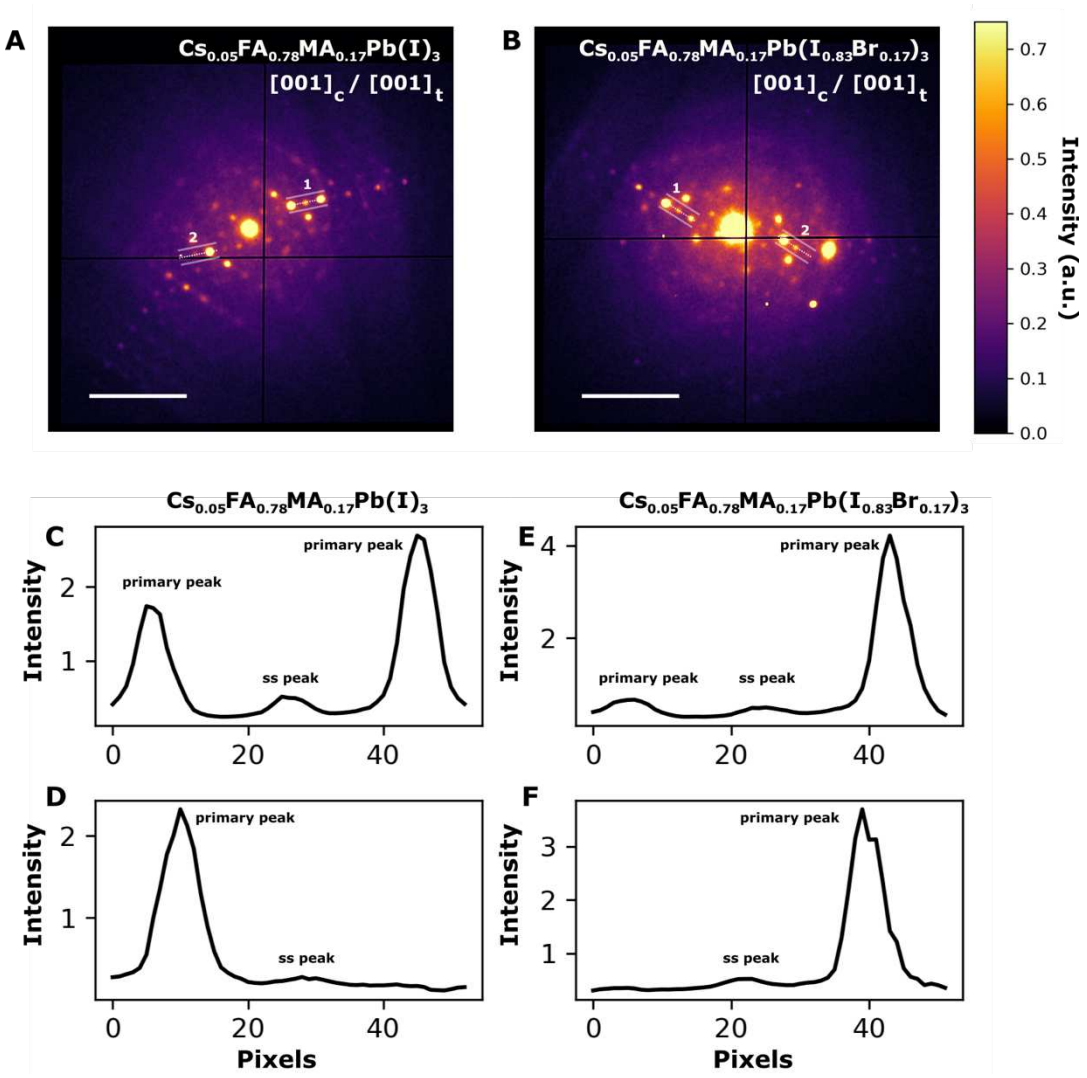

Fig. S8. Comparing observed superstructure (ss) reflections in $(Cs_{0.05}FA_{0.78}MA_{0.17})Pb(I_{0.83}Br_{0.17})_3$ and $(Cs_{0.05}FA_{0.78}MA_{0.17})PbI_3$ thin films. (A) ED pattern of $(Cs_{0.05}FA_{0.78}MA_{0.17})PbI_3$ oriented near the $[001]_c/[001]_t$ zone axis. Two regions of the diffraction pattern encompassing both primary Bragg reflections and ss reflections, chosen to extract line profiles in (C) and (D) are shown. **(B)** ED pattern of $(Cs_{0.05}FA_{0.78}MA_{0.17})Pb(I_{0.83}Br_{0.17})_3$ oriented very similarly to (A) near the $[001]_c/[001]_t$ zone axis. Two regions of the diffraction pattern encompassing both primary Bragg reflections and ss reflections, chosen to extract line profiles in (C) and (D) are shown. **(C)** Line profile extracted from region 1 in (A). Primary Bragg peaks and ss peaks are marked **(D)** Line profile extracted from 2 in (A). Primary Bragg peaks and ss peaks are marked. **(E)** Line profile extracted from region 1 in (B). Primary Bragg peaks and ss peaks are marked. **(F)** Line profile extracted from region 2 in (B). Primary Bragg peaks and ss peaks are marked. Scalebars are $0.7Å^{-1}$.

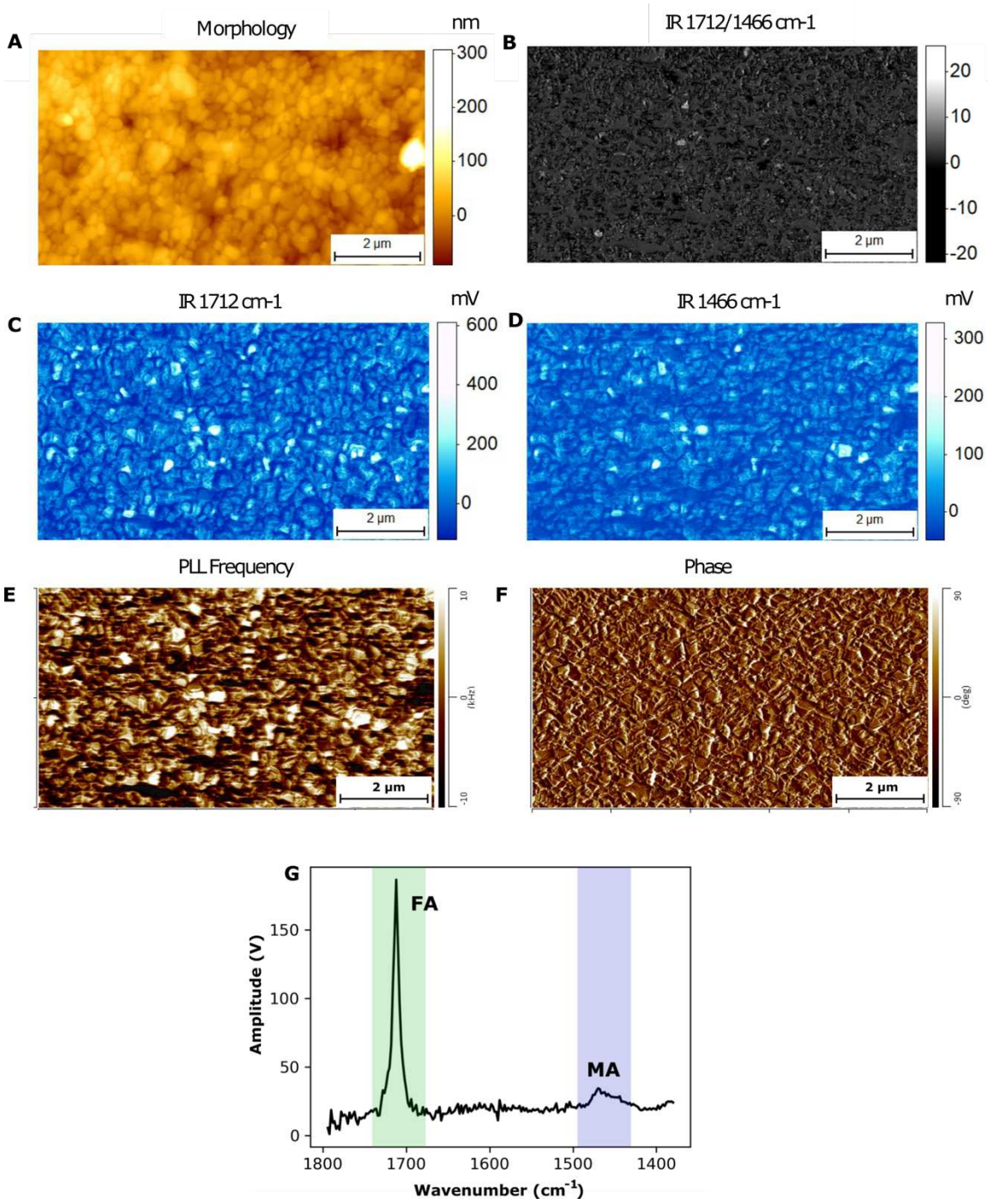

Fig. S9. AFM-IR nanospectroscopy mapping the chemical content of $(Cs_{0.05}FA_{0.78}MA_{0.17})Pb(I_{0.83}Br_{0.17})_3$. **(A)** AFM morphology map of a $(Cs_{0.05}FA_{0.78}MA_{0.17})Pb(I_{0.83}Br_{0.17})_3$ thin film, data presented in Fig. 2 is cropped from this scan area. **(B)** FA:MA ratio peak intensity map generated by dividing the FA map in (C) by the MA map in (D). **(C)** Map of the FA content (1712 cm^{-1}) and **(D)** MA content (1466 cm^{-1}). **(E)** Phase signal of the Phase Locked Loop used to track the (F) contact resonance and measure purely IR absorption. **(G)** Representative spectrum acquired from a position in (A)

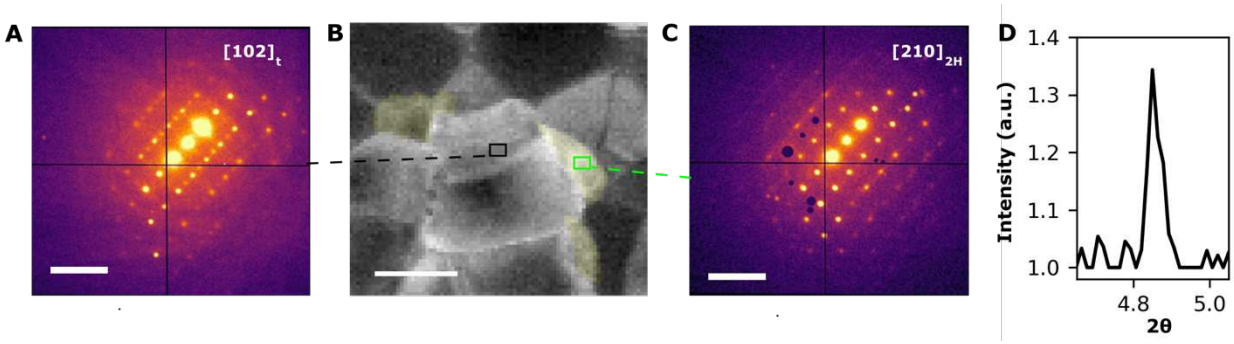

Fig. S10. Hexagonal phase impurities coexist with the main tetragonal phase in ($Cs_{0.05}FA_{0.78}MA_{0.17}$)Pb($I_{0.83}Br_{0.17}$) perovskite thin films. (A) ED pattern extracted from the black box region of interest indicated in (B) indexed to the [102] zone axis of a *P4/mbm* structure. **(B)** Annular dark field image reconstructed from ED data of a region of a triple cation film. Hexagonal phase impurities are shaded in yellow. **(C)** ED pattern extracted from the green box region of interest in dictated in (B) indexed to the [210] zone axis of a 2H hexagonal structure. Dark circles in (C) are diffraction spots from an overlapping crystal masked for clarity. **(D)** (011) Diffraction peak from the 6H hexagonal phase extracted from local nXRD measurements. Scalebars in (A) and (C) are 0.5 $Å^{-1}$. Scalebar in (B) is 100 nm.

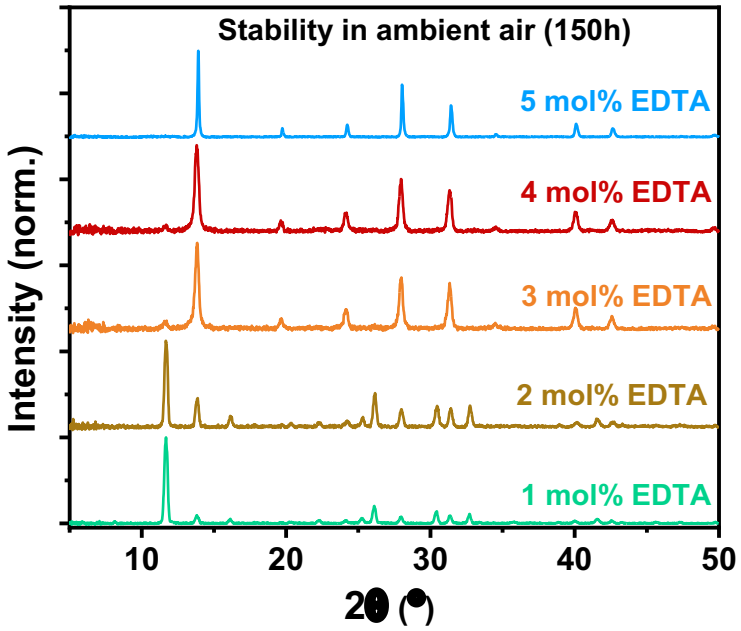

Fig. S11. XRD patterns for thin films of $FAPbI_3$ with different EDTA concentrations (mol % with respect to PbI_2) in the precursor solutions after storage of the bare films in ambient laboratory air for 150 hours.

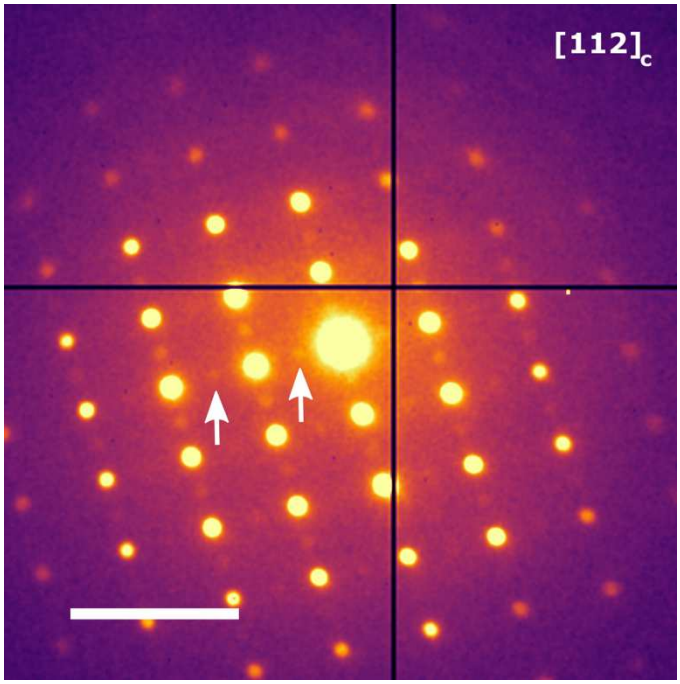

Fig. S12. Superstructure reflections indicating octahedral tilting in ots-$FAPbI_3$ (subset shown with white arrows) not consistent with the *P4/mbm* space group. Scalebar = 0.7$Å^{-1}$

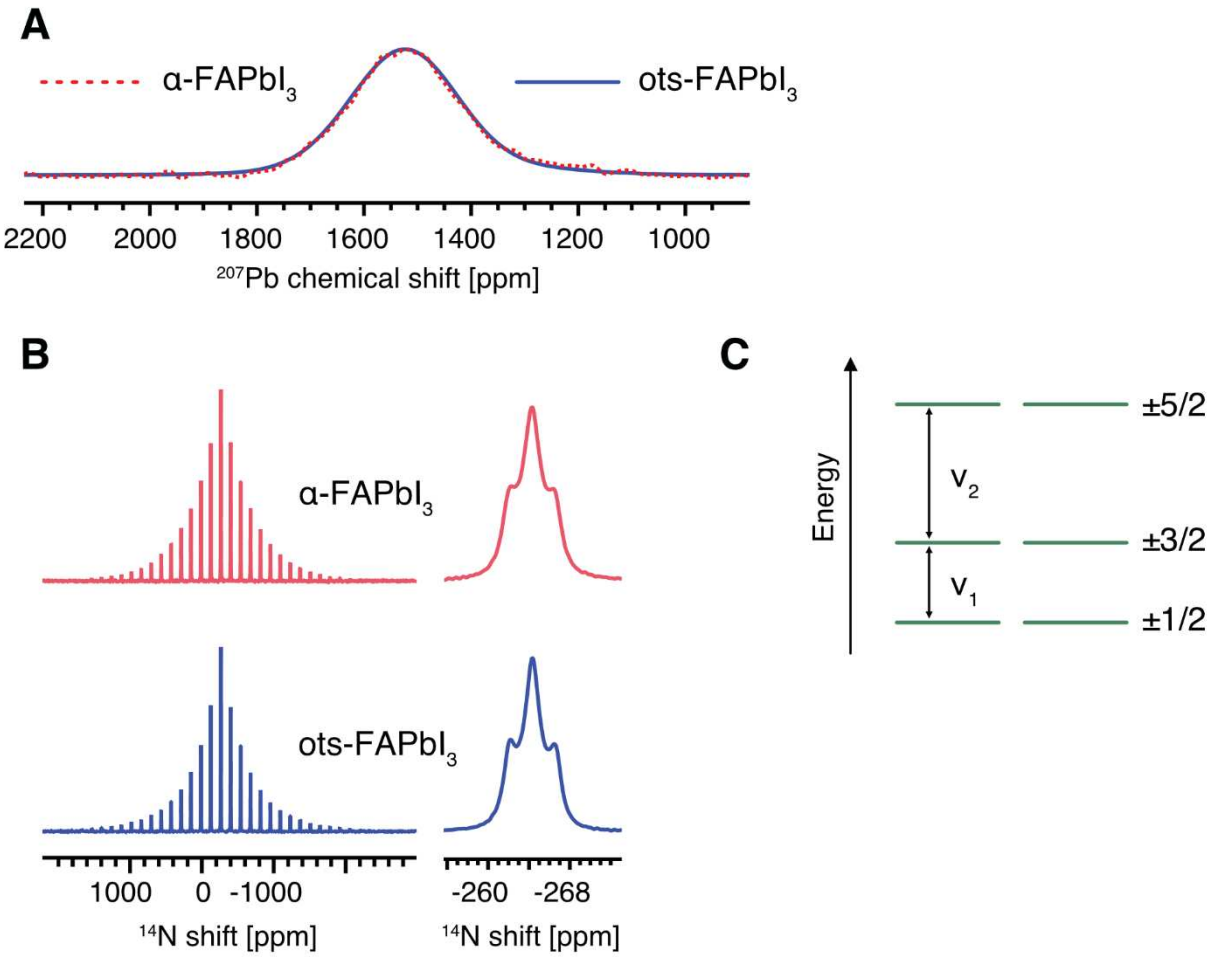

Fig. S13. (A) Solid-state ^{207}Pb NMR shows that the main component of EDTA-doped $FAPbI_3$ is α-$FAPbI_3$. **(B)** ^{14}N MAS NMR is highly sensitive to the symmetry of the A-site cation cage of the 3D perovskite phase. Here, it is not sensitive enough to detect any differences in symmetry between α-$FAPbI_3$ and ots-$FAPbI_3$. Data recorded at 4 kHz MAS (full sideband pattern, left) and 12 kHz (central peak, right). **(C)** The energy level diagram for Nuclear Quadrupole Resonance (NQR) of ^{127}I in a zero applied magnetic field. In the case of α-$FAPbI_3$, ν_1 = 86.606 MHz, ν_2 = 173.217 MHz. ±5/2, ±3/2 and ±1/2 indicate the possible spin states.

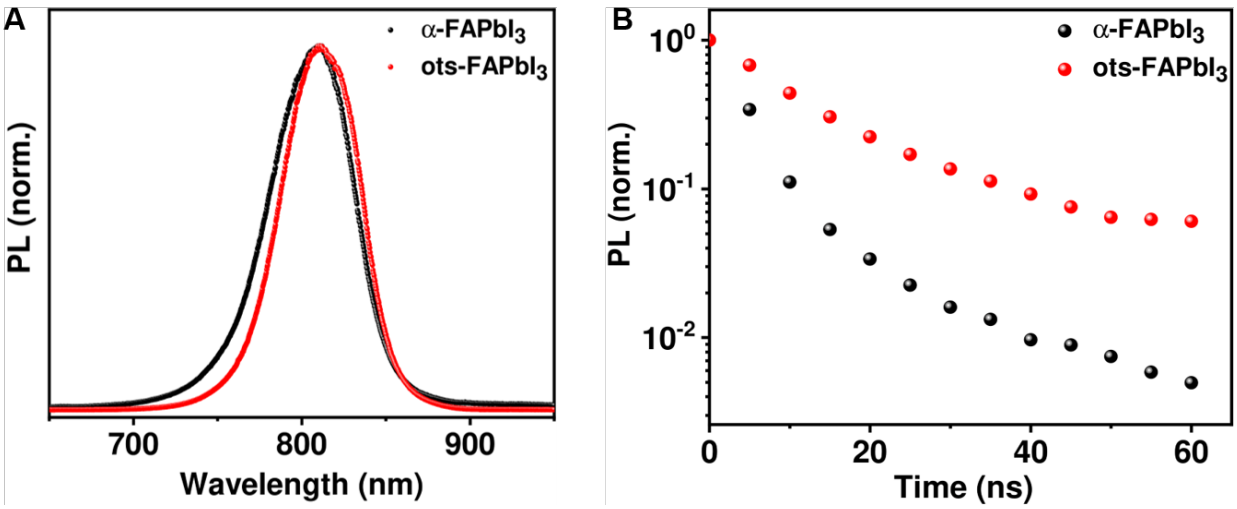

Fig. S14. (**A**) Photoluminescence of encapsulated α-$FAPbI_3$ and ots-$FAPbI_3$ thin films with excitation at 400 nm (**B**) Time-resolved photoluminescence measurements of encapsulated samples of α-$FAPbI_3$ and ots-$FAPbI_3$ films at pulsed excitation density of 0.45 μJ/cm^2/pulse and excitation wavelength of 400 nm. The lifetime, defined as the time taken to fall to 1/e of its initial intensity, at this excitation fluence is 4.4 ns for the α-$FAPbI_3$ film and 16.1 ns for the ots-$FAPbI_3$ film.

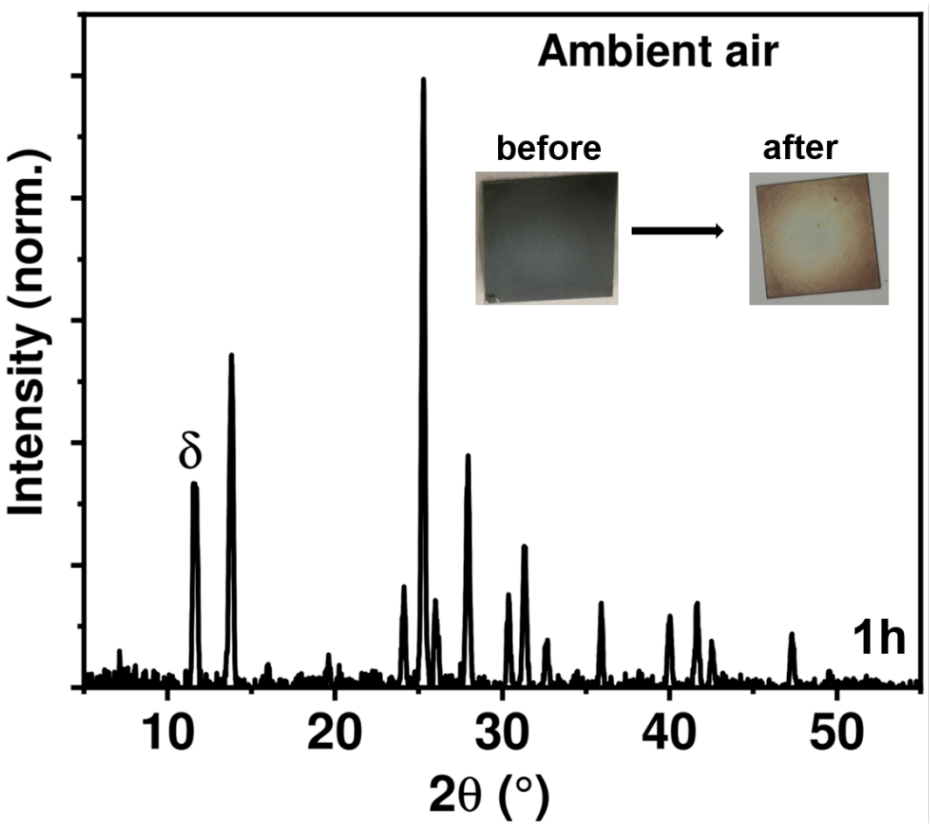

Fig. S15. X-ray diffraction (XRD) pattern for a control α-$FAPbI_3$ sample taken after exposure to ambient air for 1 hour, with the denoted δ-phase peak impurity prominent. The top left shows photographs of the films at the same time snapshots, highlighting the visible degradation.

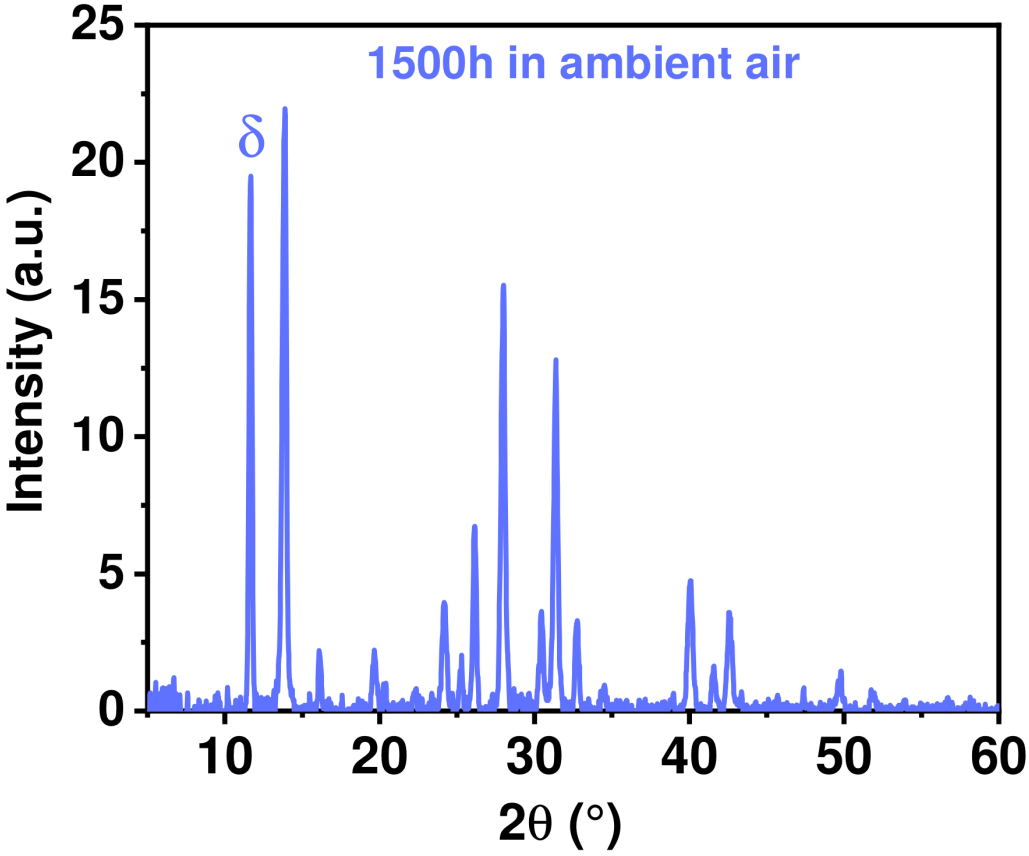

Fig. S16. XRD pattern for the ots-$FAPbI_3$ thin film shown after 1500h in ambient air.

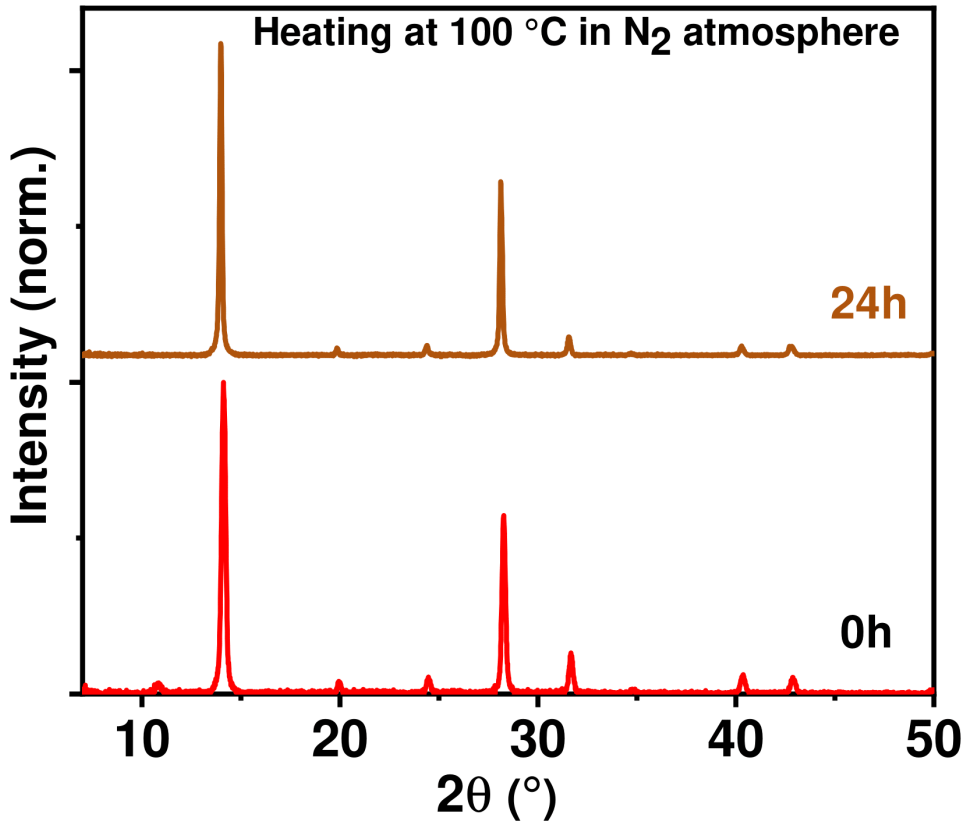

Fig. S17 XRD patterns for thin films of an ots-$FAPbI_3$ thin film before and after heating at 100 °C in N_2 atmosphere for 24 hours.

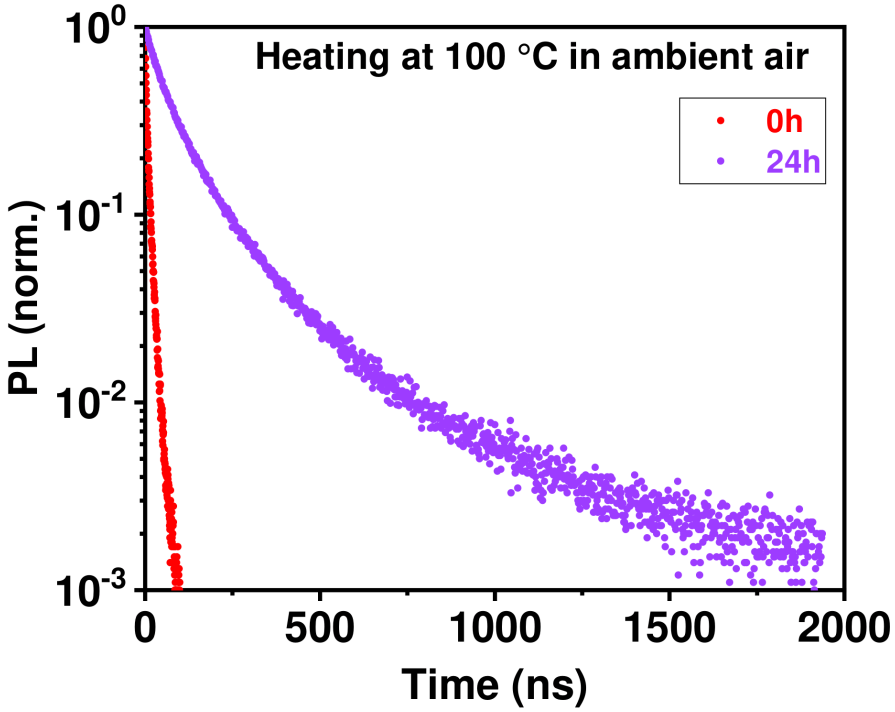

Fig. S18. TRPL of ots-$FAPbI_3$ thin films before and after heating at 100 °C in ambient air for 24 hours. The PL lifetime, defined as the time taken to fall to 1/e of its initial intensity, increases from 5.6 ns (0 h) to 83.4 ns (24 h). TRPL measurements were conducted at excitation density of 0.01 μJ/cm^2/pulse with excitation wavelength of 506 nm.

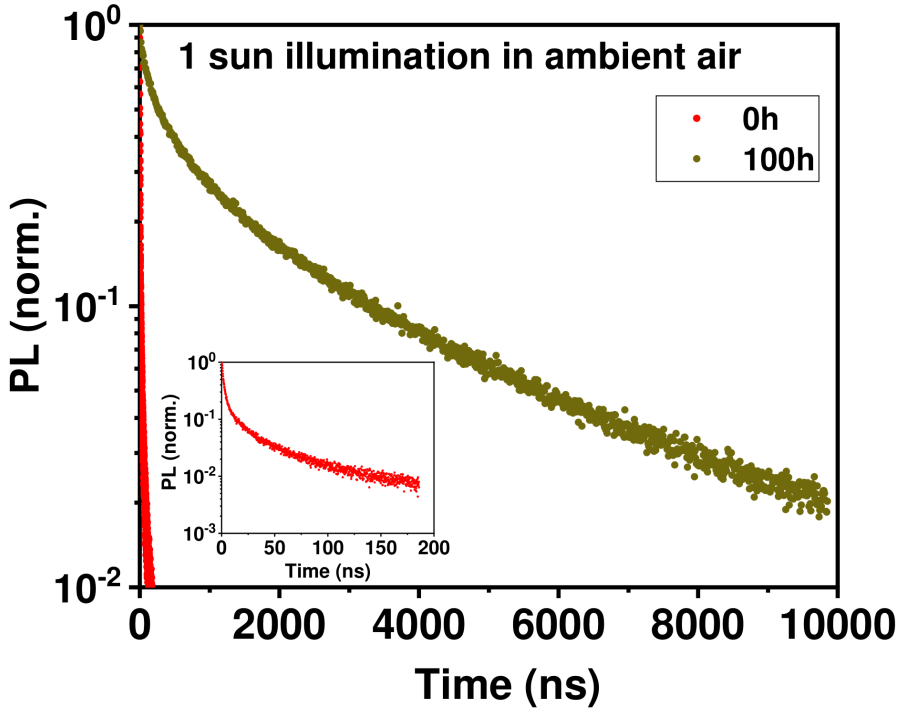

Fig. S19. TRPL for an ots-$FAPbI_3$ thin film before and after illuminating the film with 1-sun (AM1.5) in ambient air for 100 hours. The inset shows a zoom of the decay of the as-prepared film (0 h). The PL lifetime, defined as the time taken to fall to 1/e of its initial intensity, increases from 2.9 ns (0 h) to 592 ns (100 h). TRPL measurements were conducted at excitation density of 0.01 μJ/cm^2/pulse with excitation wavelength of 506 nm.

Table S1. Acquisition and processing parameters used for the solid-state NMR spectra in the main text.

^{13}C spectra

Material	Figure	T_1 [s] (relevant nucleus)	Recycle delay [s]	Number of scans	Acquisition time [h]	Lorentzian apodization [Hz]
neat EDTA	fig. 3F	11 (^{1}H)	15	5447	22.7	10
EDTA-doped $FAPbI_3$ (CP-detected)	fig. 3F/3G	6 and 40 (two components) (^{1}H)	5	45956	64	50 (in fig. 4C), 0 (in fig. 4D)
α-$FAPbI_3$ (Bloch decay)	fig. 3G	8 (^{13}C)	10	8408	23.4	0
EDTA-doped $FAPbI_3$ (Bloch decay)	fig. 3G	n.d.	10	2048	5.7	0

^{14}N spectra

Material	Figure	^{14}N T_1 [s]	Recycle delay [s]	Number of scans	Acquisition time [h]	Lorentzian apodization [Hz]
EDTA-doped $FAPbI_3$	fig. S13B	0.02	0.1	3584	0.1	10
α-$FAPbI_3$	fig. S13B	n.d.	0.1	7424	0.2	10

^{207}Pb spectra

Material	Figure	^{207}Pb T_1 [s]	Recycle delay [s]	Number of scans	Acquisition time [h]	Lorentzian apodization [Hz]
EDTA-doped $FAPbI_3$	fig. S13A	<0.1	0.1	780276	21.7	10
α-$FAPbI_3$	fig. S13A	<0.1	0.1	3328	0.1	1000

^{127}I NQR spectra

Material	Figure	^{127}I T_1 [s]	Recycle delay [s]	Number of scans	Acquisition time [h]	Lorentzian apodization [Hz]

EDTA-doped $FAPbI_3$	fig. 3H	n.d.	0.01	ν_1: 61440 (×5 offsets) ν_2: 10000 (×3 offsets)	1	ν_1: 25000 ν_2: 10000
α-$FAPbI_3$	fig. 3H	n.d.	0.01	ν_1: 10240 (×3 offsets) ν_2: 20000	0.1	ν_1: 10000 ν_2: 2000